The Astrophysical Journal, 985:62 (16pp), 2025 May 20 https://doi.org/10.3847/1538-4357/adb57d

Critical Condition of Core-collapse Supernovae. I. One-dimensional Models

David Pochik[1,2] and Todd A. Thompson[1,2,3]
[1] Center for Cosmology and Astroparticle Physics, 191 West Woodruff Avenue, Columbus, OH 43210, USA; pochik.1@buckeyemail.osu.edu
[2] Department of Physics, Ohio State University, 191 West Woodruff Avenue, Columbus, OH 43210, USA
[3] Department of Astronomy, Ohio State University, 180 West 18th Avenue, Columbus, OH 43210, USA
Received 2024 November 21; revised 2025 January 30; accepted 2025 February 11; published 2025 May 14

Abstract

When the core of a massive star collapses, neutrino heating can energize the stalled accretion shock, leading to a successful supernova. The critical condition that characterizes the transition from accretion to explosion is a central topic of study and is often characterized by a critical protoneutron star (PNS) neutrino luminosity $L_\nu^{\rm crit}$, which depends on the post-collapse mass-accretion rate $\dot{M}$ from the progenitor. We examine the critical condition by solving the spherically symmetric time-dependent Euler equations with a general equation of state and realistic microphysics for a range of $\dot{M}$, average neutrino energy $\langle\epsilon_\nu\rangle$, luminosity L_ν, PNS radius $R_\star$, mass $M_\star$, and pre-shock Mach number $\mathcal{M}$ for a fixed neutrino optical depth from the PNS surface of 2/3. We derive $L_\nu^{\rm crit}$ as a function of the input parameters. We show that increasing the pressure of the pre-shock flow, as parameterized by lowering $\mathcal{M}$, lowers the normalization of the critical condition. We connect this finding with realistic massive progenitors and show that $L_\nu^{\rm crit}$ can decrease by ∼5%–8% due to thermal changes during accretion of compositional interfaces onto the stalled shock. We test critical conditions that have been proposed in the literature, including the "antesonic" condition, the "force explosion condition," and the heuristic heating-advection timescale condition. We discuss how shock oscillations impact these critical conditions. Compared to other explosion conditions, we find that the antesonic ratio shows the least variation across the model space we explore. This work is preparatory for similar experiments in 2D axisymmetry and 3D.

Unified Astronomy Thesaurus concepts: Core-collapse supernovae (304); Hydrodynamical simulations (767)

1. Introduction

At the end of its life, a massive ($M \gtrsim 8\,M_\odot$) star's iron core rapidly collapses to high densities ($\gtrsim 10^{14}$ g cm^{-3}). The strong nuclear force becomes repulsive among the tightly packed nucleons, causing the dense core—i.e., the protoneutron star (PNS)—to "bounce" and send a shockwave through the infalling material of the star (S. A. Colgate et al. 1961). The shock is stalled by energy losses via nuclear dissociation, neutrino cooling, and ram pressure (T. J. Mazurek 1982; A. Burrows & J. M. Lattimer 1985; H. A. Bethe 1990; C. D. Ott et al. 2018). Some physical mechanism re-energizes the shock and produces a core-collapse supernova (CCSN; see, e.g., H.-T. Janka 2012; A. Burrows 2013; A. Burrows & D. Vartanyan 2021, for reviews) accompanied by a neutrino-driven wind that emanates from the PNS surface (see, e.g., Y. Z. Qian & S. E. Woosley 1996; T. A. Thompson et al. 2001; T. Prasanna et al. 2022). If the mechanism fails, stellar material continues to accrete onto the PNS until a black hole (BH) forms (potentially observed by J. Gerke et al. 2015; S. Adams et al. 2017a, 2017b; J. Neustadt et al. 2021; see also C. S. Kochanek et al. 2008).

Understanding the CCSN mechanism and how it is related to neutron star (NS) and progenitor properties is a central focus in astrophysics. A conventional explanation is the so-called "delayed neutrino mechanism" (H. A. Bethe & J. R. Wilson 1985; S. W. Bruenn et al. 1995), which continues to be studied with 3D simulations (T. Takiwaki et al. 2014; E. J. Lentz et al. 2015; T. Melson et al. 2015; H.-T. Janka et al. 2016; B. Müller et al. 2017; C. D. Ott et al. 2018; A. Summa et al. 2018; A. Burrows et al. 2020; G. Stockinger et al. 2020; A. Burrows & D. Vartanyan 2021; T. Wang & A. Burrows 2024). Because these types of simulations are computationally expensive (S. M. Couch 2017; A. Mezzacappa et al. 2020), studies are sometimes done with parameterized models with simplified neutrino schemes in 1D and 2D (A. Burrows & J. Goshy 1993; L. Scheck et al. 2006; K. Kotake et al. 2007; J. W. Murphy & A. Burrows 2008; F. Hanke et al. 2012; J. Nordhaus et al. 2012; S. M. Couch & C. D. Ott 2015), which still capture important physical properties while being much less computationally intensive.

Through the development of these simplified models, various critical conditions for explosion have been explored, which are used to distinguish exploding from nonexploding CCSN models (A. Burrows & J. Goshy 1993; O. Pejcha & T. A. Thompson 2012; J. W. Murphy & A. Burrows 2008; R. Fernández 2012; M. J. Raives et al. 2018; J. W. Murphy & J. C. Dolence 2017; M. J. Raives et al. 2021; M. Gogilashvili & J. W. Murphy 2022; M. Gogilashvili et al. 2023). Specifically, A. Burrows & J. Goshy (1993), demonstrated the existence of a critical condition for the neutrino mechanism using a spherically symmetric, time-steady configuration for the accretion flow. They showed that there exists a critical neutrino luminosity $L_\nu^{\rm crit}$ above which no stable accretion solution exists. Since then, many studies have been performed on $L_\nu^{\rm crit}$ in 1D, 2D, and 3D. These studies have revealed a nontrivial dependence of $L_\nu^{\rm crit}$ on PNS rotation and the equation of state (EoS; T. Yamasaki & S. Yamada 2005, 2006), 1D shock dynamics (R. Fernández 2012; D. Gabay et al. 2015), nuclear dissociation energy (R. Fernández et al. 2014; R. Fernández 2015), and spatial dimensionality with hydrodynamic instabilities (J. W. Murphy & A. Burrows 2008; F. Hanke et al.

2012; J. Nordhaus et al. 2012; S. M. Couch 2013; Q. A. Mabanta & J. W. Murphy 2018).

Several explanations for the physics of the critical luminosity also been proposed. One example is the heuristic timescale criterion (e.g., T. A. Thompson et al. 2005), which states that, if the time required for matter to advect through the gain region is longer than the timescale to heat the matter in the gain region, then an explosion occurs. Another is the "antesonic condition" (O. Pejcha & T. A. Thompson 2012; M. J. Raives et al. 2018, 2021), which states that, for freefall onto a standing shockwave, no time-steady accretion solutions exist if the square of the ratio of the post-shock sound speed to the escape velocity exceeds a critical value. O. Pejcha & T. A. Thompson (2012) show that this physics explains the existence of $L_\nu^{\rm crit}$ from A. Burrows & J. Goshy (1993). Another explanation for the physics of $L_\nu^{\rm crit}$ is the force explosion condition (FEC; J. W. Murphy & J. C. Dolence 2017; M. Gogilashvili & J. W. Murphy 2022; M. Gogilashvili et al. 2023), which evaluates the net integral of forces acting on the shock to determine the analytic criterion for explosion.

We investigate the physics of the 1D critical condition by developing parameterized CCSN accretion models in 1D with boundary conditions tuned to model pressurized inflow. We use model inputs that capture key details of the accretion phase and allow us to study the physics of criticality. We prescribe the PNS neutrino luminosity L_ν, neutrino spectra $\langle\epsilon_\nu\rangle$, mass-accretion rate $\dot{M}$, PNS radius $R_\star$, PNS mass $M_\star$, neutrino optical depth τ, and outer boundary Mach number $\mathcal{M}$ as inputs for our models. The last parameter captures the thermal content of the pre-shock, infalling stellar material. Note that 1D accretion models are typically constructed with pressureless or near-pressureless freefall ($\mathcal{M} \gg 1$) in the pre-shock region (R. Fernández 2012; O. Pejcha & T. A. Thompson 2012; D. Gabay et al. 2015; M. J. Raives et al. 2018, 2021). However, the fluid above the shock has nonzero pressure in realistic progenitors (S. E. Woosley et al. 2002; S. E. Woosley & A. Heger 2007). As an example, O. Pejcha & T. A. Thompson (2012) showed that the antesonic condition is reduced when the pre-shock fluid is pressurized, and thus the pre-shock pressure may directly affect the condition(s) for explodability.

In particular, previous works show that, when the Si/O layer accretes onto the stalled shock, the ram pressure $P_{\rm ram}$ and $\dot{M}$ decrease, which either drives the model closer to criticality or directly leads to explosion (C. D. Ott et al. 2013; C. D. Ott et al. 2018; D. Vartanyan et al. 2018; T. Wang et al. 2022). However, changes in the thermal content of the accreting material may affect criticality as well. Accretion of mass with higher pressure will lead to smaller infall velocity at the shock. Both will affect explodability (O. Pejcha & T. A. Thompson 2012). The changes in $P_{\rm ram}$ have been highlighted in Si/O layer studies, but the changes in the thermal content, such as the entropy S of the infalling material, have received less attention. These changes may map into the critical condition in a nontrivial way. It is possible that the changes in both $\dot{M}$ and S across compositional boundaries may independently impact the critical neutrino luminosity when the boundaries accrete onto the shock. In Section 3.6, we explore how our accretion models respond to changes in the thermal content using parameters motivated by realistic massive star progenitors.

Here, we extend the analysis performed by previous studies. Our primary goals are (1) to understand the physics of various explosion conditions and their connections to the neutrino heating mechanism, (2) to understand why the critical condition changes as a function of the controlling parameters, and (3) to prepare a framework for future 2D and 3D critical condition studies. Prior studies show that the normalization of the critical curve depends on τ (R. Fernández 2012), neutrino properties, and PNS properties (O. Pejcha & T. A. Thompson 2012), but they do not show why the critical condition depends on these and other parameters. Moreover, some accretion studies (O. Pejcha & T. A. Thompson 2012; D. Gabay et al. 2015; M. J. Raives et al. 2018, 2021) have not captured the effects of $\mathcal{M}$ on the shock dynamics. We investigate the role of both the finite pre-shock pressure (i.e., low $\mathcal{M}$) and other controlling parameters on criticality in our time-dependent models.

In Section 2, we introduce the numerical tools for this study. Section 2.1 introduces the hydrodynamics equations. The governing equations for neutrino–matter interactions and composition rates are covered in Section 2.2. The boundary and initial conditions are covered in Sections 2.3 and 2.4, respectively. Section 3 begins our discussion on results. Specifically, Section 3.1 shows our fiducial accretion models with their dependence on $\mathcal{M}$ and L_ν. Section 3.2 introduces our procedure for finding the critical curve and includes a discussion of shock dynamics, and Section 3.2.1 covers the functional dependence of $L_\nu^{\rm crit}$ on the controlling parameters. Section 3.3 covers our results on the antesonic condition, Section 3.4 shows our results on the advection and heating timescales, and Section 3.5 shows our findings on the FEC. Section 3.6 discusses the behavior of $\mathcal{M}$ in criticality studies that use realistic progenitors. We conclude with Section 4.

2. Numerical Framework

We use the 3D radiative magnetohydrodynamics (MHD) code Athena++ (J. M. Stone et al. 2020), including a general EoS (F. X. Timmes & F. D. Swesty 2000; M. S. Coleman 2020) and neutrino microphysics (see, e.g., L. Scheck et al. 2006). All calculations here are spherically symmetric, and spatial discretization is performed in Athena++ with a second-order piecewise parabolic method (P. Colella & P. R. Woodward 1984). The fluxes at cell boundaries are determined with the Harten–Lax–van Leer contact (or HLLC; E. F. Toro et al. 1994) Riemann solver. For temporal integration, we use the second-order-accurate van Leer predictor–corrector algorithm (J. M. Stone & T. Gardiner 2009) with the corner transport upwind method of P. Colella (1990) along with a second-order strong-stability-preserving Runge–Kutta method constrained by a Courant–Friedrichs–Lewy number of CFL = 0.3. We discretize the computational domain into $n_R = 256$ radial zones with logarithmic spacing. We observe changes in $L_\nu^{\rm crit}$ on the order of 1% or less when changing n_R between values of 128 and 512, and thus we do not examine other radial resolutions for the studies outlined in this paper.

2.1. Hydrodynamics

We solve the fully compressible Euler equations for the conservation of mass, momentum, and energy:

$$\frac{\partial \rho}{\partial t} + \nabla \cdot (\rho\, \boldsymbol{v}) = 0, \tag{1}$$

$$\frac{\partial (\rho \boldsymbol{v})}{\partial t} + \nabla \cdot (\rho \boldsymbol{v} \otimes \boldsymbol{v}) + \nabla P = -\rho \frac{GM_\star}{r^2}\hat{r}, \tag{2}$$

$$\frac{\partial E}{\partial t} + \nabla \cdot [(E + P)\mathbf{v}] = \mathcal{L}_{\rm net}, \tag{3}$$

where ρ is the mass density, $\boldsymbol{v}$ is the velocity vector, P is the pressure, r is the radius, G is Newton's constant, $E = \rho\epsilon$ is the total energy density, and $\mathcal{L}_{\rm net} = \rho\dot{Q} = \rho(\dot{Q}_{\rm H} - \dot{Q}_{\rm C})$ is the net energy deposition rate per unit volume due to neutrino–matter interactions.

2.2. Microphysics

The PNS is excised and replaced with an inner boundary at $R_\star \geqslant 30$ km in our calculations, therefore $\rho \lesssim 10^{12}\,{\rm g\,cm^{-3}}$ near the inside boundary (see Section 2.3 for details on inner boundary conditions). We do not include an EoS for dense nuclear matter, because of the relatively low inner boundary ρ, but we still require an EoS that captures the transition for electrons (e^-) and positrons (e^+) from relativistic to non-relativistic regimes, since the temperature T varies from a few MeV to tenths of an MeV for $r \in [R_\star,\ 1000\ {\rm km}]$. Using the general EoS framework in Athena++ developed by M. S. Coleman (2020), Equations (1), (2), and (3) are closed with a general EoS for e^-, e^+, photons, and nonrelativistic baryons, based on tabular interpolation of the Helmholtz free energy (F. X. Timmes & F. D. Swesty 2000).

The electron-type charged-current processes dominate energy exchange and electron fraction Y_e evolution in the accretion flow (H. T. Janka 2000):

$$e^- + p \leftrightarrow n + \nu_e, \tag{4}$$

$$e^+ + n \leftrightarrow p + \bar{\nu}_e. \tag{5}$$

We spatially and temporally resolve Y_e by solving the source function for electron-type charged-current processes (Y. Z. Qian & S. E. Woosley 1996):

$$v_r \frac{dY_e}{dr} = \lambda_{\nu_e n} + \lambda_{e^+ n} - (\lambda_{\nu_e n} + \lambda_{e^+ n} + \lambda_{\bar{\nu}_e p} + \lambda_{e^- p})Y_e, \tag{6}$$

where $v_r = |\mathbf{v}|$ in spherical symmetry. The forward and reverse reaction rates are provided by Y. Z. Qian & S. E. Woosley (1996):[4]

$$\lambda_{\nu_e n} \approx \frac{1+3\alpha^2}{2\pi^2}(\hbar c)^2 G_{\rm F}^2 \frac{L_{\nu_e}}{R_\star^2} \times \left(\epsilon_{\nu_e} + 2\Delta + \frac{\Delta^2}{\langle\epsilon_{\nu_e}\rangle}\right)(1 - x), \tag{7}$$

$$\lambda_{\nu_e p}^{-} \approx \frac{1+3\alpha^2}{2\pi^2}(\hbar c)^2 G_{\rm F}^2 \frac{L_{\nu_e}^{-}}{R_\star^2} \times \left(\epsilon_{\nu_e}^{-} - 2\Delta + \frac{\Delta^2}{\langle\epsilon_{\nu_e}^{-}\rangle}\right)(1 - x), \tag{8}$$

$$\lambda_{e^- p} \approx 0.448 \quad T_{\rm MeV}^5 \quad \frac{F_4(\eta_{\rm e})}{F_4(0)}, \tag{9}$$

$$\lambda_{e^+ n} \approx 0.448 \quad T_{\rm MeV}^5 \quad \frac{F_4(-\eta_{\rm e})}{F_4(0)}, \tag{10}$$

(in units of $\rm s^{-1}$) where $\alpha = 1.26$ is the axial coupling vector, $G_{\rm F}^2 = 1.16637 \times 10^{-11}\,{\rm MeV^{-2}}$ is the Fermi constant, $\hbar$ is the reduced Planck's constant, c is the speed of light, $\epsilon_\nu = \langle\epsilon_\nu^2\rangle/\langle\epsilon_\nu\rangle$ is a ratio of neutrino energy moments, L_ν is the neutrino luminosity, $\Delta = 1.2935\,{\rm MeV}$ is the neutron–proton mass difference, $\eta = \mu/k_B T$ is the degeneracy parameter of a given species with chemical potential μ, $x = \sqrt{1 - R_\star^2/r^2}$, $T_{\rm MeV} = T/1\,{\rm MeV}$, and $F_n(\eta)$ is the Fermi integral:

$$F_n(\eta) = \int_0^\infty dx\, \frac{x^n}{\exp[x - \eta] + 1}. \tag{11}$$

The neutrino energy moments in general are given by (T. A. Thompson et al. 2001)

$$\langle\epsilon_\nu^n\rangle = \frac{\int_{-1}^{1} d\mu \int \epsilon_\nu^n f_\nu(r,\, t,\, \epsilon_\nu,\, \mu) d^3\epsilon_\nu}{\int_{-1}^{1} d\mu \int f_\nu(r,\, t,\, \epsilon_\nu,\, \mu) d^3\epsilon_\nu}, \tag{12}$$

where

$$f_\nu(r,\, t,\, \epsilon_\nu,\, \mu) = g_\nu(r,\, t,\, \mu) [\times [1 + \exp(\epsilon_\nu/k_b T_\nu - \eta_\nu)]^{-1}, \tag{13}$$

and g_ν is an angle-dependent function (L. Scheck et al. 2006). Equation (12) can be simplified to show how $\langle\epsilon_{\nu_e}\rangle$ depends on the neutrino temperature T_ν (L. Scheck et al. 2006):

$$\langle\epsilon_\nu^n\rangle = (k_B T_\nu)^n \frac{F_{n+2}(\eta_\nu)}{F_2(\eta_\nu)}, \tag{14}$$

where we set $\eta_{\nu_e} = \eta_{\bar{\nu}_e} = 0$. The net neutrino heating rate per unit mass $\dot{Q} = \dot{Q}_{\rm H} - \dot{Q}_{\rm C}$ is given by modified versions of the Y. Z. Qian & S. E. Woosley (1996) rates:

$$\dot{Q}_{\rm H} \approx 9.65\, N_A X_n\, L_{\nu_e,51}\, \epsilon_{\nu_e,{\rm MeV}}^2 + X_p\, L_{\bar{\nu}_e,51}\, \epsilon_{\bar{\nu}_e,{\rm MeV}}^2 \frac{1-x}{R_{\star,6}^2}, \tag{15}$$

$$\dot{Q}_{\rm C} \approx \frac{2.27\, N_A}{F_5(0)} T_{\rm MeV}^6 (X_p\, F_5(\eta_e) + X_n\, F_5(-\eta_e)), \tag{16}$$

(in units of $\rm MeV\,s^{-1}g^{-1}$) where N_A is Avogadro's constant, $X_p = Y_e$ is the proton fraction, $X_n = 1 - Y_e$ is the neutron fraction, $L_{\nu,51} = L_\nu/10^{51}\,{\rm erg\,s^{-1}}$, $\epsilon_{\nu,{\rm MeV}}^2 = \langle\epsilon_\nu^3\rangle/\langle\epsilon_\nu\rangle/1\,{\rm MeV}$, and $R_{\star,6} = R_\star/10^6$ cm. We set $L_{\nu_e} = L_{\bar{\nu}_e} = L_\nu$ everywhere, and we modify the rates of Y. Z. Qian & S. E. Woosley (1996) by implementing $\eta_e \neq 0$ where applicable, e.g., Equations (9), (10), and (16) (T. A. Thompson et al. 2001). Note that the post-shock radius at which $\dot{Q} > 0$ is the gain radius $R_{\rm gain}$, and the area between $R_{\rm gain}$ and the shock radius $R_{\rm shock}$ is the "gain region" (H. A. Bethe & J. R. Wilson 1985). Above $R_{\rm shock}$, the charged-current interactions (Equations (4) and (5)) are suppressed because of the low free-nucleon fraction of the infalling material. Primarily $Y_e = 26/56 \sim 0.46$ material ($\rm Fe^{56}$ nuclei) falls onto the shock during accretion, which changes to $Y_e \sim 0.5$ once the Si/O layer accretes onto the shock (see Section 3.6 for more details on compositional layers). The compositional changes across the shock are not inherently captured in the Helmholtz EoS, and hence we modify the heating/cooling and reaction rates with the free-nucleon mass fraction from Y. Z. Qian & S. E. Woosley (1996) to model the

[4] See Appendix D in L. Scheck et al. (2006) for a detailed derivation for both the reaction rates and neutrino heating/cooling rates covered in this section.

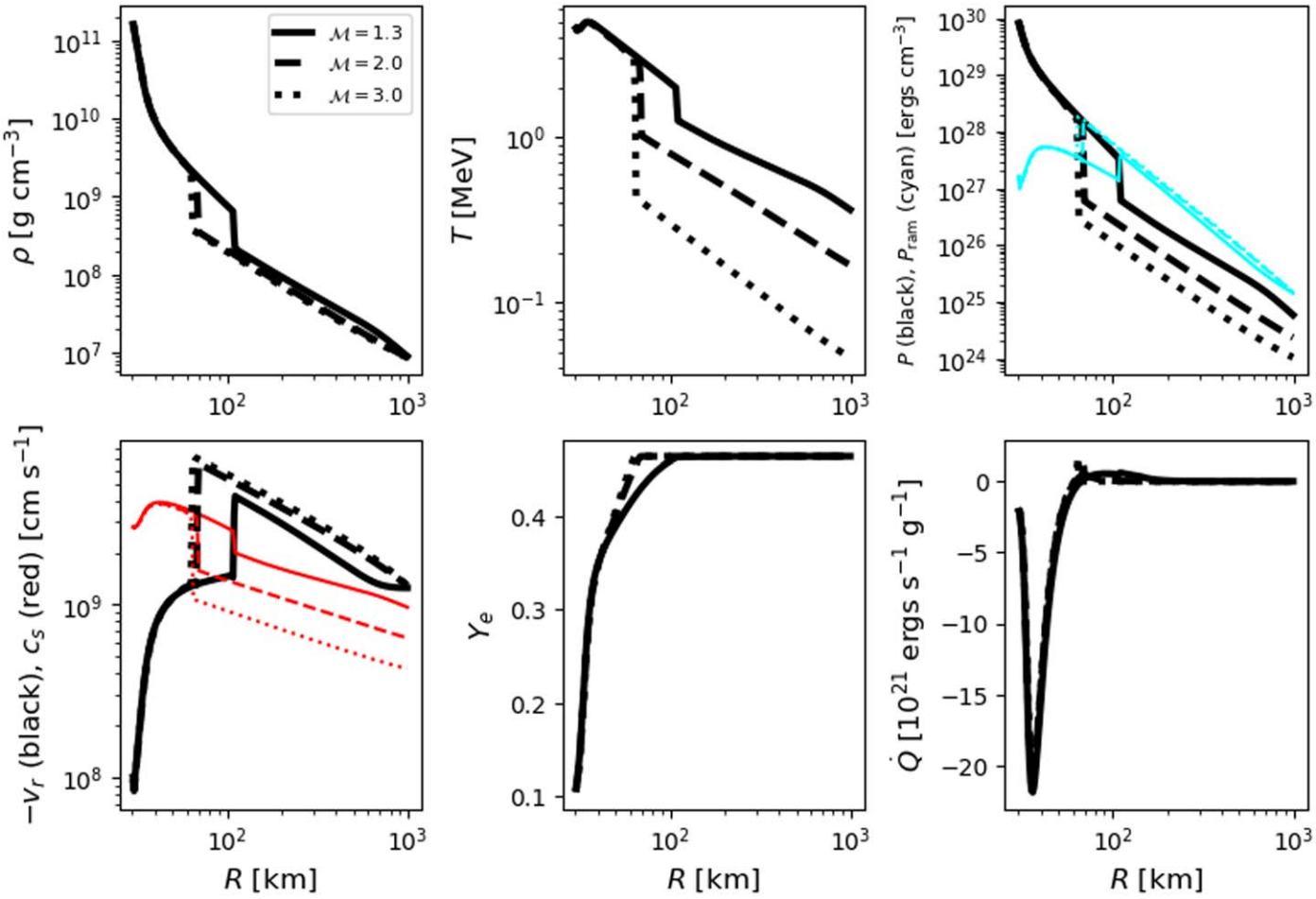

Figure 1. Steady-state profiles with fiducial inputs at $L_\nu = 30 \times 10^{52}$ and $\dot{M} = 0.7\ M_\odot\ \mathrm{s}^{-1}$ for ρ, T, P, v_r, Y_e, and $\dot{Q}$ using $\mathcal{M} = 1.3$ (solid), 2.0 (dashed), and 3.0 (dotted). The red profiles in the bottom-left panel are c_s, and the cyan profiles in the top-right panel are $P\mathrm{b}_{\rm ram}$. $R_{\rm shock}$ is characterized by the strong discontinuity in the profiles, which is where the accretion flow transitions from super- to subsonic. Due to the strong $\sim T^6$ dependence in $\dot{Q}_C$, the steep drop in T across the shock leads to a sharp increase in $\dot{Q}$ just behind the shock. Because the EoS does not intrinsically capture the transition between nuclei and free nucleons across the shock, we use χ_N to reduce $\dot{Q}$ to zero at $r > R_{\rm shock}$. However, this treatment is less effective for $\mathcal{M} = 1.3$, where $\dot{Q}$ slowly approaches zero in the pre-shock region.

suppression in $\dot{Q}$ at $r > R_{\rm shock}$:

$$\chi_N = 828\ \frac{T_{\rm MeV}^{9/8}}{\rho_8^{3/4}} \exp\left(-\frac{7.074}{T_{\rm MeV}}\right), \tag{17}$$

where $\rho_8 = \rho/10^8\ \mathrm{g\,cm^{-3}}$. Equations (15) and (16) are multiplied by $\min(\chi_N,\ 1)$. The steep drop in T at $r > R_{\rm shock}$ causes χ_N to rapidly decrease, which approximately models the drop in $\dot{Q}$ across the shock. This treatment is effective for a wide parameter space, but it sometimes does not effectively decrease the pre-shock $\dot{Q}$. In some regimes, the pre-shock $\dot{Q}$ slowly drops to zero instead of being immediately driven to zero by χ_N, as shown in Figures 1 and 2.

Finally, following (R. Fernández 2012), we suppress the heating, cooling, and Y_e number rates at high density using

$$f_{\rm sup} = \exp(-\rho/\rho_0), \tag{18}$$

where ρ_0 is the inner boundary density from the initial condition (IC) profile.

2.3. Boundary Conditions

Since we implement a second-order spatial integration method in Athena++, we apply two ghost zones at the inner (denoted as "gi") and outer (denoted as "go") boundaries of the computational domain. For simplicity, ρ, Y_e, v_r, T, and P are constant across the ghost zones for a given time step. We enforce inflow boundary conditions to model accretion, e.g., $Y_{e,\rm gi}$ and $v_{r,\rm gi}$ are equal to their respective first active zone quantities. We compute $T_{\rm gi}$ by finding an equilibrium temperature $T_{\rm eq}$ that satisfies $\dot{Q}(\rho, T_{\rm eq}, Y_e) \sim 0$ in the first active zone, then we set $T_{\rm gi} = T_{\rm eq}$.

It is important that we maintain constant τ for all stable models, because the normalization of the critical curve is a function of τ (R. Fernández 2012). We define τ as

$$\tau = \int_{R_\star}^{R_{\rm out}} dr\ N_A \sigma_{\nu_e} X_n \rho, \tag{19}$$

where $R_{\rm out}$ is the outer boundary, and

$$\sigma_{\nu_e} = \sigma_0 \left(\frac{1+3\alpha^2}{4}\right) \frac{(\langle \epsilon_{\nu_e}^2 \rangle + 2\Delta \langle \epsilon_{\nu_e} \rangle + \Delta^2)}{(m_e c^2)}, \tag{20}$$

is the electron neutrino cross section (L. Scheck et al. 2006) with $\sigma_0 \sim 1.76 \times 10^{-44}\ \mathrm{cm}^2$. Because ρ drops significantly across the shock, the flow at $r < R_{\rm shock}$ dominates the integral for τ and the upper limit reduces from $R_{\rm out}$ to $R_{\rm shock}$. Given our assumption of optically thin neutrino heating and cooling, the

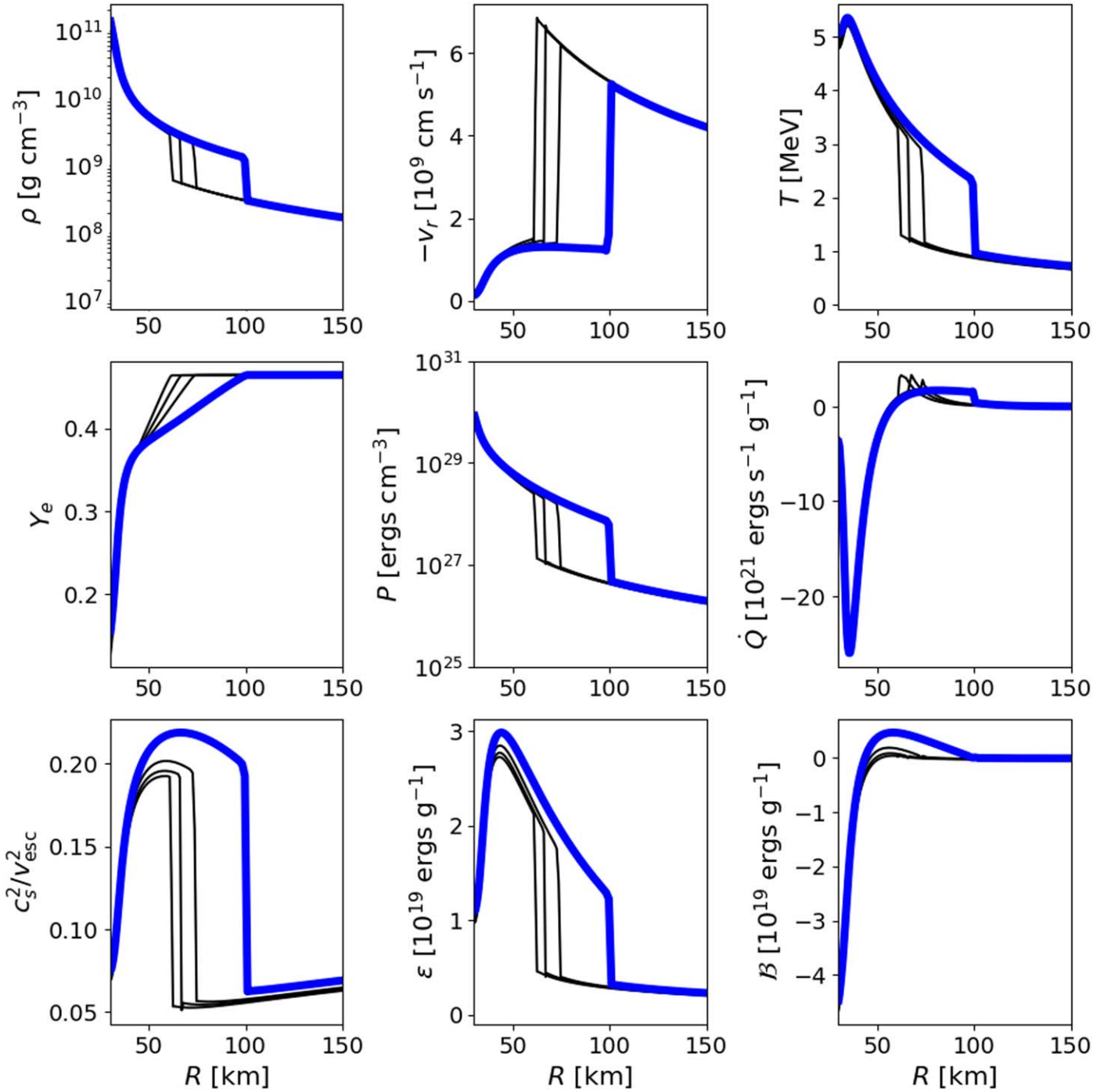

Figure 2. Time-steady solutions for ρ, v_r, T, Y_e, P, $\dot{Q}$, the antesonic ratio $c_s^2/v_{\rm esc}^2$, ϵ, and the Bernoulli integral $\mathcal{B}$ from a series of simulations using $\dot{M} = 1.0\,M_\odot$ s^{-1} and $\mathcal{M} = 2.0$ with fiducial inputs. The black profiles show model evolution as L_ν is increased over the range $[50,\ 70] \times 10^{51}$ erg s^{-1} in increments of 10^{51} erg s^{-1}. The blue profile is evaluated at $L_\nu = 77 \times 10^{51}$ erg s^{-1}, which is just beneath $L_\nu^{\rm crit}$. The bottom-right panel shows positive $\mathcal{B}$ values in the post-shock region for stable models. For the lower L_ν models shown here (black profiles), χ_N does not fully suppress $\dot{Q}$ in the immediate post-shock region, causing $\dot{Q}$ to smoothly approach zero at larger radii.

neutrino optical depth up to the shock is $\tau \sim 2/3$. We maintain this value by manipulating the ghost-zone density values. First, we set a fixed density value ρ_0 in the ghost zones and calculate τ. Once the physical time sufficiently exceeds the post-shock sound crossing time, i.e., $t \gtrsim t_{\rm sound} \sim r/c_s \sim 10^{-2}$ s, τ is checked via Equation (19). If $\tau \leqslant 2/3 - \delta_\tau$ or $\tau \geqslant 2/3 + \delta_\tau$, where $\delta_\tau = 2.0 \times 10^{-3}$, $\rho_{\rm gi}$ is increased or decreased by $(1 + 3.0 \times 10^{-3})$ times its current value. Once another sound crossing time passes and the post-shock flow has settled from the perturbation in $\rho_{\rm gi}$, Equation (19) is recalculated and τ is checked again. This process iterates until the threshold $2/3 - \delta_\tau < \tau < 2/3 + \delta_\tau$ is met. This results in a time-steady numerical simulation with $\tau \sim 2/3$ and allows us to consistently map the critical curve.

At the outer boundary, $R_{\rm out} = 1000$ km, $\rho_{\rm go}$, $Y_{e,{\rm go}}$, and $v_{r,{\rm go}}$ are set equal to their respective values from the steady-state IC

profile, whereas $T_{\rm go}$ is set equal to the final active zone temperature. $P_{\rm go}$ is set with the Mach number $\mathcal{M} = v_r/c_s$ at the outer boundary (R. Fernández & C. Thompson 2009):

$$P_{\rm go} = \frac{\rho_{\rm go}(\epsilon_{\rm go} + c^2)}{\frac{\Gamma_{\rm go}\mathcal{M}^2c^2}{v_{r,\rm go}^2} - 1} \sim \frac{\rho_{\rm go}v_{r,\rm go}^2}{\Gamma_{\rm go}\mathcal{M}^2}, \tag{21}$$

where $\Gamma_{\rm go} = \Gamma(\rho,\ T,\ Y_e)_{\rm go}$ is the adiabatic index, and $\epsilon_{\rm go} = \epsilon\,(\rho,\ T,\ Y_e)_{\rm go}$ is the total specific energy. Both quantities are interpolated from the EoS using the ghost-zone quantities. $\mathcal{M} > 1$ is a free parameter that controls the thermal content of the accreted matter, which directly affects the normalization of $L_\nu^{\rm crit}$ (Section 3.2.1). As $\mathcal{M}$ increases above unity, the pre-shock flow becomes supersonic and P (Equation (21)) decreases. For $\mathcal{M} \gg 1.0$, P ahead of the shock becomes negligible and the pre-shock flow approaches freefall. Note that supersonic flow must always be maintained at the outer boundary for accretion models, otherwise near- or subsonic flow becomes disrupted by pressure waves and prevents the fine-tuning of $\dot{M}$.

We specify $\dot{M}$ with the cell-centered outer boundary density $\rho_{\rm out}$ and velocity $v_{r,\rm out}$ from the IC profile via $\dot{M} = 4\pi\rho_{\rm out}R_{\rm out}^2|v_{r,\rm out}|$.[5] We keep L_ν and $\langle\epsilon_\nu\rangle$ constant as the models evolve, and these parameters are manipulated only at the start of simulations. Note that we have tested our models with a feature that slowly increases L_ν during the simulation and observed no qualitative change in $L_\nu^{\rm crit}$ compared to our current procedure.

To simplify the parameter studies discussed in Sections 3 through Sections 3.5, we specify a mass number $\bar{A} = 1$ in the EoS over all r. However, to examine the changes in $L_\nu^{\rm crit}$ due to the accretion of compositional interfaces of realistic massive progenitors, we use a somewhat different approach for both $\bar{A}$ and the outer boundary condition in Section 3.6. Instead of using $\bar{A} = 1$ everywhere, we use $\bar{A} = 56$ (for Fe nuclei) between the shock and the outer boundary and $\bar{A} = 1$ (for free nucleons) for $r < R_{\rm shock}$. With this modification, we can make a more realistic mapping between the entropy profiles of realistic progenitors and the thermal content of the accreting material in our models.

2.4. Initial Condition

We initialize our models with a numerical steady-state accretion profile generated with Athena++. Following previous works (see, e.g., R. Fernández 2012; O. Pejcha & T. A. Thompson 2012), we select values for P ($\sim 10^{30}$ erg cm^{-3}), ρ ($\sim 10^{11}$ g cm^3), Y_e ($\sim 1.0 \times 10^{-1}$), T ($\sim$4 MeV), and v_r (-10^8 cm s^{-1}) that are appropriate for the PNS surface. The outer boundary P ($\sim 10^{24}$ erg cm^{-3}), ρ (10^7 g cm^{-3}), Y_e ($\sim$26/56), T ($\sim$0.1 MeV), and v_r (-10^9 cm s^{-1}) are selected to match the "pre-shocked" quantities in realistic progenitors (S. E. Woosley et al. 2002; S. E. Woosley & A. Heger 2007). The stalled shock is located at 50 km $\lesssim R_{\rm shock} \lesssim$ 200 km, which depends on the input physics. Our fiducial models use inputs of $R_\star = 30$ km, $M_\star = 1.4\,M_\odot$, $\langle\epsilon_{\nu_e}\rangle \simeq 12.6$ MeV, and $\langle\epsilon_{\bar{\nu}_e}\rangle \simeq 18.9$ MeV, which correspond to $T_{\nu_e} = 4$ MeV and $T_{\bar{\nu}_e} = 6$ MeV, respectively (R. Fernández 2012). We maintain $\langle\epsilon_{\bar{\nu}_e}\rangle/\langle\epsilon_{\nu_e}\rangle = 1.5$ throughout our analysis, and we keep the average energies constant when varying L_ν. We vary the fiducial parameters to understand how the critical condition depends on PNS properties (see Sections 3.2 and 3.2.1) and $\mathcal{M}$ (see Sections 3.3, 3.4, and 3.5).

We generate a numerical accretion model (see Section 3.1) and evolve it in Athena++. An initial transient occurs and the model is driven toward time-steady flow. We evolve nonexploding models up to $t = 3$ s to ensure stability. Steady-state accretion is defined by $\tau \sim 2/3$ (see Section 2.3) with a stationary shock. Our definition of a "stationary" shock is one that maintains either (1) $V_{\rm shock}(t) = 0$ (stable, nonoscillatory) or (2) $V_{\rm shock}(t) \neq 0$ but $\langle V_{\rm shock}\rangle_t \sim 0$ (stable, oscillatory; see Section 3.2). If $V_{\rm shock}$ becomes nonzero or changes sign any time after $t = 2.4$ s but does not explode, the model is flagged as stable and oscillatory. This is similar to the work done by D. Gabay et al. (2015), where they observe oscillatory but stable accretion models at low $\dot{M}$. Once a stable model fulfills these criteria, it is used as a "checkpoint" in the $L_\nu - \dot{M}$ plane, and we progress to a new L_ν or $\dot{M}$ by using the stabilized model as the new IC profile. At constant $\dot{M}$, we increase L_ν step by step, which results in either a new steady-state configuration or an explosion. The latter is characterized by the moment when the shock advects through the outer boundary and $v_{r,\rm out} > 0$.

3. Results

Here, we analyze the results from our parameterized 1D accretion models (see Section 3.1 for a fiducial model set). We use these results both to examine the diagnostic tools that distinguish between stable and exploding models and to understand the importance of the input parameters in critical condition studies. We investigate the classic critical condition (Sections 3.2 and 3.2.1), the antesonic condition (Section 3.3), the heuristic heating and cooling timescale condition (Section 3.4), and the force explosion condition (Section 3.5). The results shown in Sections 3.1, 3.3, 3.4, and 3.5 examine $\mathcal{M}$ dependence but otherwise use fiducial input parameters. We also address the implications of compositional boundaries accreting onto the shock for the critical condition (Section 3.6).

3.1. Fiducial Models

In Figure 1, we show time-steady fiducial solutions that share the same inputs, except we vary $\mathcal{M} = 1.3,\ 2.0,\ 3.0$ at $r = 1000$ km, which maps to pre-shock Mach numbers, e.g., $\mathcal{M}_{\rm preshock} \sim 2,\ 4,\ 6.5$, respectively, that are similar to those found in other works (see E. Abdikamalov et al. 2016, 2018). We have selected this range in $\mathcal{M}$ both to illustrate the effect of significant pre-shock pressure ($\mathcal{M} = 1.3$) and to show how the critical condition converges as the pre-shock flow asymptotically approaches pressureless freefall at high $\mathcal{M}$. Note that, in Section 3.6, we use $\bar{A} = 56$ at the outer boundary, which allows us to examine a wider range in $\mathcal{M}$ for the incoming pre-shock flow and to make more realistic comparisons with progenitor models.

Over the range of $\mathcal{M}$ that we test, we find that our accretion models and the critical condition changes with $\mathcal{M}$. All else being equal, larger $\mathcal{M}$ drives down the pre-shock P (Equation (21)), T, and c_s. Meanwhile, $P_{\rm ram} = \rho v_r^2$ ahead of the shock increases and drives the shock to smaller radii. This places the accretion solution in a more stable regime, which

[5] Note that we are using cell-centered fluid variables here, but $R_{\rm out} = 1000$ km is a face-valued quantity. We find this inconsistency to be quantitatively negligible in our critical condition results.

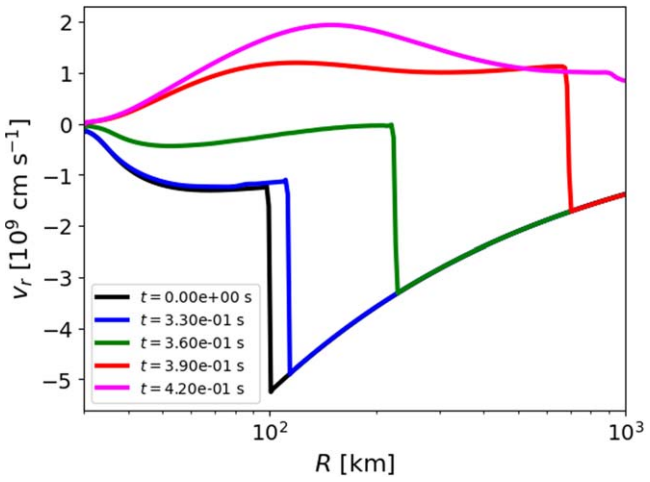

Figure 3. v_r profiles for the exploding model, $L_\nu^{\rm crit} = 77.2 \times 10^{51}$ erg s^{-1}, from the series shown in Figure 2. The magenta profile at $t = 4.2 \times 10^{-1}$ s is the beginning of the wind phase.

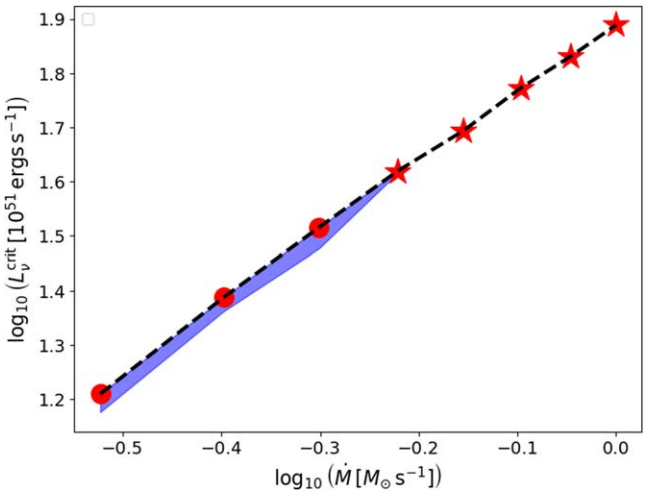

Figure 4. Critical curve for $\mathcal{M} = 2.0$ with fiducial inputs. Red dots represent models with strong shock oscillations that lead into explosions. Red stars are explosions that occur without oscillations. The blue shaded area shows regions with stable oscillatory models, while elsewhere under the curve is occupied by stable nonoscillatory models with the same fiducial inputs.

then requires larger $L_\nu^{\rm crit}$ to become unstable and explode. Note that $R_{\rm shock}$ decreases from $R_\star \sim 112$ km to $R_\star \sim 69$ km for $\mathcal{M} = 1.3 \rightarrow 2.0$ and from $R_\star = 69$ km to $R_\star \sim 64$ km for $\mathcal{M} = 2.0 \rightarrow 3.0$, which shows that the flow ahead of the shock is approaching freefall and further increasing $\mathcal{M}$ has less impact on the dynamics. We find that this convergence to pressureless freefall manifests in all critical condition results at high $\mathcal{M}$ (see Sections 3.2.1, 3.3, 3.4, and 3.5).

In Figure 2, we increase L_ν over the range $[50, 77] \times 10^{51}$ erg s^{-1} for a model using fiducial inputs with $\dot{M} = 0.5\,M_\odot$ s^{-1} and $\mathcal{M} = 2.0$ until nearly achieving an explosion. As L_ν increases, this corresponds directly to an increase in $\dot{Q}$ (Equation (15)) and other thermal quantities in the post-shock region, and the shock moves toward larger radii. Here, the final stable model is at $L_\nu = 77 \times 10^{51}$ erg s^{-1}, which is represented by the blue line in Figure 2. Once $L_\nu^{\rm crit} = 77.2 \times 10^{51}$ erg s^{-1} is reached (Figure 3), the flow destabilizes and the model explodes. The model transitions from accretion to explosion, where the shock travels outward and advects past $R_{\rm out}$. When this happens, $v_{r,\rm out}$ transitions from negative (inflow) to positive (outflow), which defines the explosion phase.

3.2. Critical Curve

For a fixed $\dot{M}$, $\mathcal{M}$, $M_\star$, $\langle \epsilon_{\nu_e} \rangle$, and $R_\star$, we increase L_ν by $\Delta L_\nu = 0.2 \times 10^{51}$ erg s^{-1} and evolve our accretion models until they achieve either nonoscillatory stability, oscillatory stability, or an explosion. When a model explodes, we set $L_\nu = L_\nu^{\rm crit}$, and we define near-critical $L_\nu^{\rm crit,n}$ models as those that are nearest to explosion and remain subcritical. The critical values for the studies outlined in Sections 3.3, 3.4, and 3.5, are determined from $L_\nu^{\rm crit,n}$ models, because the calculations in these studies break down once stable accretion is no longer sustained. Otherwise, we use the first exploding model,[6] $L_\nu^{\rm crit}$, for the discussions in this section and Section 3.2.1.

$L_\nu^{\rm crit}$ is shown in Figure 4 for $\mathcal{M} = 2.0$. In agreement with prior critical curve studies, we find that $L_\nu^{\rm crit}$ monotonically increases with $\dot{M}$. Similarly to D. Gabay et al. (2015), we observe stable oscillatory models just beneath $L_\nu^{\rm crit}$ for low $\dot{M}$. Figure 5 shows the behavior of $R_{\rm shock}$ and $V_{\rm shock}$ for oscillating models. Note that the oscillations do not dampen during $t = 3$ s, and we observe strong shock oscillations for models with $R_\star = 50$ km.

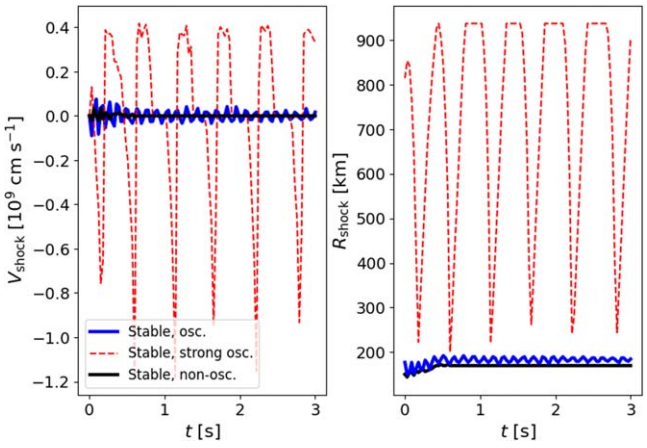

Figure 5. Examples of stable and oscillatory accretion solutions. Left: shock velocities $V_{\rm shock}$ for models of varying time-dependent characteristics. All models here use $M_\star = 1.4\,M_\odot$ and $\langle \epsilon_{\nu_e} \rangle \simeq 12.6$ MeV. The stable, nonoscillatory profile (solid black) uses $\mathcal{M} = 1.3$, $\dot{M} = 0.4\,M_\odot$ s^{-1}, $R_\star = 30$ km, and $L_\nu = 17.0 \times 10^{51}$ erg s^{-1}. The stable, oscillatory profile (solid blue) uses $\mathcal{M} = 1.3$, $\dot{M} = 0.4\,M_\odot$ s^{-1}, $R_\star = 30$ km, and $L_\nu = 17.4 \times 10^{51}$ erg s^{-1}. The stable model with strong oscillations (dashed red) uses $\mathcal{M} = 2.0$, $\dot{M} = 0.6\,M_\odot$ s^{-1}, $R_\star = 50$ km, and $L_\nu = 10.4 \times 10^{51}$ erg s^{-1}. All models undergo an initial transient for the first few hundred ms, but the blue and red profiles continue oscillating for the duration of the simulation while the black model achieves a perfect numerical steady state. Right: shock radii for the same simulations. $R_{\rm shock}$ stabilizes at ∼150–200 km for the black and blue profiles, while the the red model oscillates at ∼600 km.

We find that the shock dynamics change as a function of $\mathcal{M}$. For $\mathcal{M} = 1.3$, a stable oscillatory model occurs at high $\dot{M}$, specifically at $\dot{M} = 1.0\,M_\odot$ with $L_\nu^{\rm crit,n} = 49.8 \times 10^{51}$ erg s^{-1}. Meanwhile, no oscillations occur for models with $\dot{M} = 0.3\,M_\odot$ s^{-1} and $\mathcal{M} = 3.0$. For some models with fiducial inputs, we also observe: (1) shock oscillations at $L_\nu^{\rm crit}$ but no

[6] Note that rerunning the same models may produce different $L_\nu^{\rm crit}$ values at most by ∼1%.

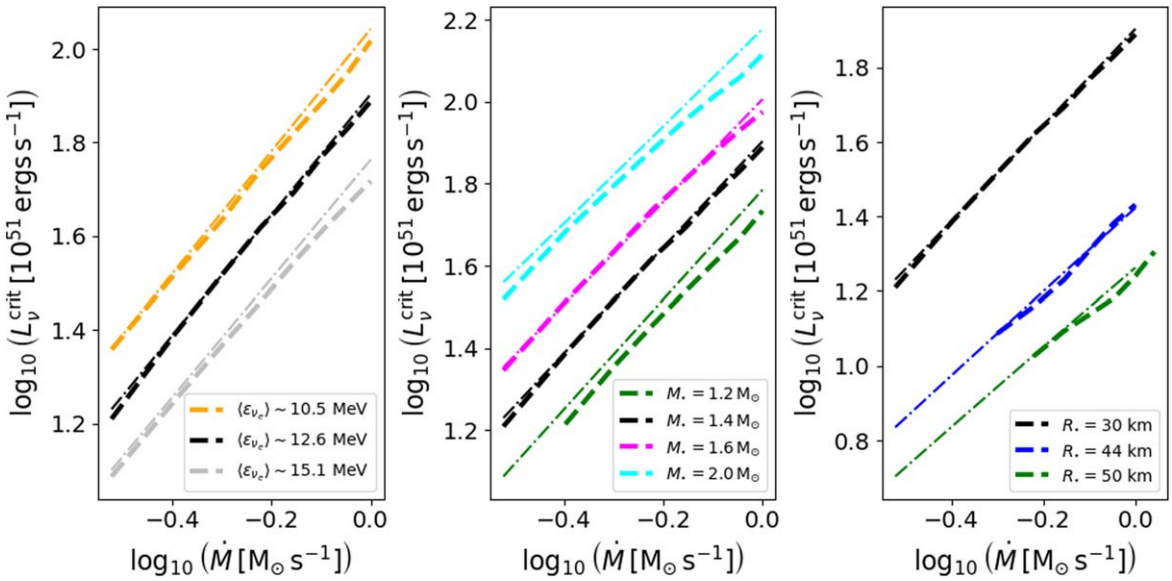

Figure 6. $L_\nu^{\rm crit}$–$\dot{M}$ analysis for various input parameters at $\mathcal{M} = 2.0$. Left: $L_\nu^{\rm crit}$ at $R_\star = 30$ km and $M_\star = 1.4\,M_\odot$ with $\langle\epsilon_{\nu_e}\rangle \simeq 10.5$ MeV (orange), $\langle\epsilon_{\nu_e}\rangle \simeq 12.6$ MeV (black), and $\langle\epsilon_{\nu_e}\rangle \simeq 15.1$ MeV (gray). Middle: $L_\nu^{\rm crit}$ at $R_\star = 30$ km and $\langle\epsilon_{\nu_e}\rangle \simeq 12.6$ MeV with $M_\star = 1.2\,M_\odot$ (green), $M_\star = 1.4\,M_\odot$ (black), $M_\star = 1.6\,M_\odot$ (magenta), and $M_\star = 2.0\,M_\odot$ (cyan). Right: $L_\nu^{\rm crit}$ at $M_\star = 1.4\,M_\odot$ and $\langle\epsilon_{\nu_e}\rangle \simeq 12.6$ MeV with $R_\star = 30$ km (black), $R_\star = 44$ km (blue), and $R_\star = 50$ km (green). The thin dashed–dotted lines with corresponding colors are the linear fittings provided by Equation (22).

oscillations for models at $L_\nu < L_\nu^{\rm crit}$ (e.g., models at $\dot{M} = 0.5\,M_\odot\ {\rm s^{-1}}$ and $\mathcal{M} = 1.3$), and (2) no shock oscillations at $L_\nu^{\rm crit}$, but shock oscillations for models at $L_\nu < L_\nu^{\rm crit}$ (e.g., models at $\dot{M} = 0.6\,M_\odot\ {\rm s^{-1}}$ and $\mathcal{M} = 2.0$).

3.2.1. Critical Curve Dependence on Inputs

We determine the power-law scalings of $L_\nu^{\rm crit}$ with respect to the input parameters (shown in Figures 6 and 7) by using a least-squares method to fit $L_\nu^{\rm crit}$ as a function of $\dot{M}$, $R_\star$, $M_\star$, and $\langle\epsilon_{\nu_e}\rangle$, which yields the following scaling relation:

$$L_\nu^{\rm crit} = 32.8\left(\frac{\dot{M}}{0.5M_\odot\,{\rm s^{-1}}}\right)^{1.29}\left(\frac{R_\star}{30\ {\rm km}}\right)^{n_{R_\star}} \times\left(\frac{M_\star}{1.4M_\odot}\right)^{n_{M_\star}}\left(\frac{\langle\epsilon_{\nu_e}\rangle}{12.6\ {\rm MeV}}\right)^{n_\epsilon} 10^{51}\ {\rm erg\ s^{-1}}. \quad (22)$$

We find that the power laws weakly depend on $\dot{M}$, where

$$n_{R_\star} = -2.58\left(\frac{\dot{M}}{0.5\,M_\odot\ {\rm s^{-1}}}\right)^{0.16}, \quad (23)$$

$$n_{M_\star} = 1.97\left(\frac{\dot{M}}{0.5\,M_\odot\ {\rm s^{-1}}}\right)^{-0.15}, \quad (24)$$

and

$$n_\epsilon = -1.69\left(\frac{\dot{M}}{0.5\,M_\odot\ {\rm s^{-1}}}\right)^{0.06}. \quad (25)$$

Equations (22)–(25) are scaled with respect to one of the fiducial models at $\mathcal{M} = 2.0$. Figure 8 shows how these terms change with $\dot{M}$. The scaling term $n_{M_\star}$ decreases with $\dot{M}$, but the other terms positively trend with $\dot{M}$. We anticipate that these power laws may also depend on $R_\star$, $M_\star$, and $\langle\epsilon_\nu\rangle$.

For the data in Figure 6, we select the following inputs: $\langle\epsilon_{\nu_e}\rangle \in [10.5,\ 15.1]$ MeV to capture the range of neutrino energies prevalent in CCSNe during accretion (T. A. Thompson et al. 2003; L. Scheck et al. 2006), $M_\star \in [1.2,\ 2.0]\,M_\odot$ to match

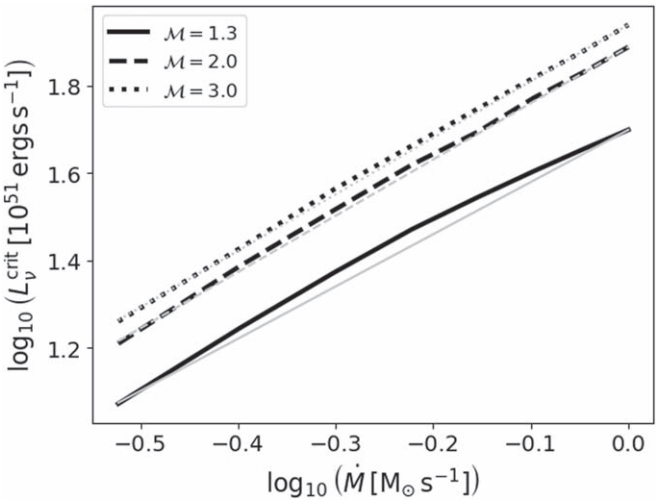

Figure 7. Critical curves with fiducial inputs for $\mathcal{M} = 1.3$ (solid), $\mathcal{M} = 2.0$ (dashed), and $\mathcal{M} = 3.0$ (dotted). The gray profiles with corresponding line styles are the linear fittings provided by Equation (22). Each linear fitting is scaled with $L_\nu^{\rm crit}$ data at $\dot{M} = 0.5\,M_\odot\ {\rm s^{-1}}$ from each value of $\mathcal{M}$.

the range of observations of NS masses (M. Ferreira & C. M. C. Providência 2021), and $R_\star \in [30,\ 50]$ km to capture a range of radii during the early accretion phase after collapse (A. Burrows & J. M. Lattimer 1986). Figure 6 shows how $L_\nu^{\rm crit}$ changes with the input parameters. Increasing $\langle\epsilon_{\nu_e}\rangle$ causes $L_\nu^{\rm crit}$ to drop because $\langle\epsilon_{\nu_e}^3\rangle/\langle\epsilon_{\nu_e}\rangle$ enters in Equation (15) and directly controls the amount of neutrino heating behind the shock. Higher $\langle\epsilon_{\nu_e}\rangle$ leads to higher $\dot{Q}_H$ at fixed L_ν, and thus lower $L_\nu^{\rm crit}$ is required for explosion. Increasing $M_\star$ causes $R_{\rm shock}$ to decrease, which leads to a higher post-shock T, a higher escape velocity, and more effective neutrino cooling. Higher $L_\nu^{\rm crit}$ is thus required to cause an explosion for higher $M_\star$. Finally, the heating rate drops with radius as $1/R_\star^2$ (Equation (15)). However, increasing $R_\star$ shifts the post-shock region to larger radii, which decreases T behind the shock. $\dot{Q}_c$ decreases more rapidly with $R_\star$ than $\dot{Q}_H$

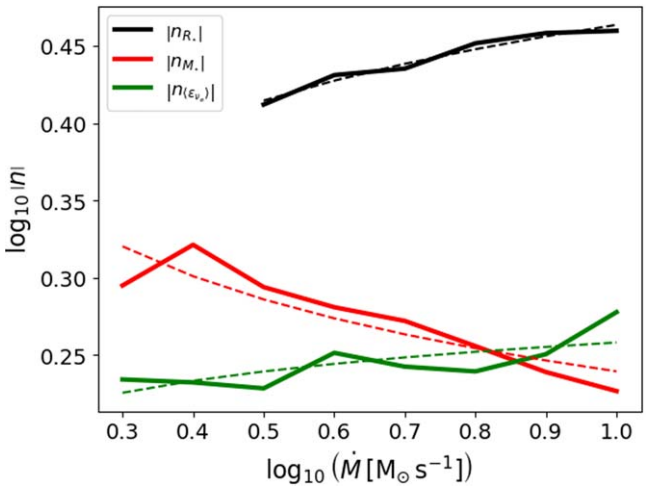

Figure 8. Absolute value of $L_\nu^{\rm crit}$ power-law scaling terms n for $R_\star$ (solid black, Equation (23)), $M_\star$ (solid red, Equation (24)), and $\langle\epsilon_{\nu_e}\rangle$ (solid green, Equation (25)) as functions of $\dot{M}$. The dashed lines show the linear fits to the data.

because $\dot{Q}_C$ sensitively depends on T (Equation (16)). Because this drives the accretion flow closer to an explosive regime, $L_\nu^{\rm crit}$ decreases with larger $R_\star$.

As discussed in Section 3.1, $L_\nu^{\rm crit}$ increases with the outer boundary $\mathcal{M}$. Once $\mathcal{M}$ is sufficiently high ($\mathcal{M} \gtrsim 3.0$), the pre-shock accretion asymptotically approaches freefall. Increasing $\mathcal{M}$ further does not qualitatively change the dynamics, and $L_\nu^{\rm crit}$ becomes unaffected. Our results show that $L_\nu^{\rm crit}$ increases on average by $\sim$44% and $\sim$12% for $\mathcal{M} = 1.3 \rightarrow 2.0$ and $\mathcal{M} = 2.0 \rightarrow 3.0$, respectively (see Figure 7 and Table 1). We support this result by scaling Equation (22) with $\mathcal{M} = 1.3$ and $\mathcal{M} = 3.0$ data, where Table 1 shows $L_\nu^{\rm crit}$ converging with respect to $\mathcal{M}$ for both Equation (22) and the numerical data. Note that the decrease in the normalization of $L_\nu^{\rm crit}$ for $\mathcal{M} = 2.0 \rightarrow 1.3$ is on the order of the decrease in $L_\nu^{\rm crit}$ due to the multidimensional instabilities studied in J. W. Murphy & A. Burrows (2008) and S. M. Couch (2013) ($\sim$30% decrease when comparing 1D data to 2D/3D data).

Note that O. Pejcha & T. A. Thompson (2012) have derived a scaling relation for $L_\nu^{\rm crit}$ with their fiducial model, where they find $L_\nu^{\rm crit,PT} \sim M_\star^{1.84}\,\dot{M}^{0.723}\,R_\star^{-1.61}$. Because the power laws themselves depend on $\dot{M}$ (Equations (23)–(25)), we find that $L_\nu^{\rm crit}$ from Equation (22) scales approximately the same as $L_\nu^{\rm crit,PT}$ with either $R_\star$ or $M_\star$ when either $\dot{M} = 0.03\,M_\odot\ \mathrm{s}^{-1}$ or $\dot{M} = 0.7\,M_\odot\ \mathrm{s}^{-1}$, respectively. Otherwise, we find that $L_\nu^{\rm crit}$ in our framework depends more sensitively on the inputs, which may be due to the following physical differences: (1) we assume L_ν is constant for all r, whereas O. Pejcha & T. A. Thompson (2012) include L_ν produced by the accreting matter; (2) in the pre-shock region, we set $P \neq 0$ with $\mathcal{M}$, while O. Pejcha & T. A. Thompson (2012) set $P = 0$; and (3) our models are time-dependent, while the models by O. Pejcha & T. A. Thompson (2012) are time-independent.

O. Pejcha & T. A. Thompson (2012) also derive a toy analytic condition on $L_\nu^{\rm crit}$. The toy model suggests that it scales linearly with $\dot{M}$ and $M_\star$ while having an inverse-square dependence on $R_\star$. Their model uses a simple relativistic EoS $\left(\epsilon = \frac{3P}{\rho}\right)$ with pressureless freefall, basic scaling relations for neutrino heating and cooling (e.g., $H \sim 1/r^2$ and $C \sim 1/r^4$), and $\frac{dY_e}{dr} = 0$. In our models, we implement a general EoS with finite pre-shock P and a heating function that requires $Y_e(r)$ and $\langle\epsilon_{\nu_e}\rangle$ as input. These physical differences change the normalization of $L_\nu^{\rm crit}$, which leads to the stronger scaling with the inputs shown in Figures 6 and 7.

3.3. Antesonic Condition

O. Pejcha & T. A. Thompson (2012) and M. J. Raives et al. (2018, 2021) have shown that, for pressureless freefall onto a standing accretion shock with an isothermal post-shock medium, there exists a critical condition on the post-shock isothermal sound speed c_T,

$$\frac{(c_T^{\rm crit})^2}{v_{\rm esc}^2} = \frac{3}{16} = 0.1875, \tag{26}$$

where $v_{\rm esc}$ is the escape velocity. Above this critical value of the "antesonic ratio," there are no solutions that simultaneously satisfy the strong shock jump conditions and the time-steady fluid equations in the post-shock flow for this model problem. The name "antesonic" comes from the fact that this critical value is reached before the sonic condition in a trans-sonic isothermal Parker wind ($c_s^2/v_{\rm esc}^2 = 1/4$). M. J. Raives et al. (2018) showed that, once the critical antesonic ratio in Equation (26) is exceeded, the system undergoes a time-dependent transition from accretion to explosion and drives a thermal wind. Further, M. J. Raives et al. (2018) generalized the antesonic condition to a Γ law EoS of the form $P \propto \rho^\Gamma$ and pressureless freefall, obtaining a critical antesonic ratio of $c_s^2/v_{\rm esc}^2 = 3\Gamma/16$, which was obtained numerically by O. Pejcha & T. A. Thompson (2012).

Because we are using a general EoS with finite pre-shock pressure, there likely does not exist an analytic derivation of the antesonic condition in our framework (M. J. Raives et al. 2018). In their steady-state calculations with a general EoS and neutrino heating/cooling, O. Pejcha & T. A. Thompson (2012) showed numerically that $\max(c_s^2/v_{\rm esc}^2) \simeq 0.21$ is the maximum value of the antesonic condition, it occurs near $R_{\rm gain}$ in an individual profile, and it holds along the critical curve.

In order to assess the antesonic condition in our time-dependent simulations, we sample numerically stable models at $L_\nu^{\rm crit,n}$ for $\mathcal{M} = 1.3$, $\mathcal{M} = 2.0$, and $\mathcal{M} = 3.0$, and we evaluate the maximum antesonic ratio for $R_\star \leqslant r \leqslant R_{\rm shock}$. For non-oscillatory stable models, we compute the maximum ratio once steady state is reached. For oscillatory stable models, we first evaluate the ratio at its post-shock maximum for all time t, then compute its average in t. We plot the maximum antesonic ratio for near-critical models in Figure 9. Note that the bars at each point indicate the true maximum value achieved for each simulation. This shows that time-dependent dynamics may temporarily drive the antesonic ratio above its critical value, but the model maintains stability.

O. Pejcha & T. A. Thompson (2012) show that the critical antesonic ratio for models with accretion luminosity and a pre-shock freefall velocity of $v_{\rm ff} = 0.5 v_{\rm esc}$ remains roughly constant along the critical luminosity curve. However, we find that the value of $\max(c_s^2/v_{\rm esc}^2)$ increases as a function of $\dot{M}$ (and $L_\nu^{\rm crit,n}$) by $\sim$5% for $\mathcal{M} = 1.3$, $\sim$3% for $\mathcal{M} = 2.0$, and $\sim$4% for $\mathcal{M} = 3.0$, and that the near-critical ratio ranges between $\sim$0.205 and 0.225 (see Figure 9). To illustrate this, Figure 10

Table 1
Fractional Increase in $L_\nu^{\rm crit}$

$\dot{M}$ [$M_\odot$ s^{-1}]	0.3	0.4	0.5	0.6	0.7	0.8	0.9	1.0	AVG
$\mathcal{M}_1 = 1.3,\ \mathcal{M}_2 = 2.0$ (data)	0.37	0.39	0.39	0.41	0.41	0.47	0.50	0.54	0.44
$\mathcal{M}_1 = 2.0,\ \mathcal{M}_2 = 3.0$ (data)	0.12	0.10	0.12	0.11	0.13	0.11	0.12	0.12	0.12
$\mathcal{M}_1 = 1.3,\ \mathcal{M}_2 = 2.0$ (eqn.)	0.32	0.36	0.39	0.41	0.43	0.45	0.47	0.48	0.42
$\mathcal{M}_1 = 2.0,\ \mathcal{M}_2 = 3.0$ (eqn.)	0.11	0.11	0.12	0.12	0.12	0.12	0.12	0.12	0.12

Notes. Fractional increase in $L_\nu^{\rm crit}$, i.e., $|L_\nu^{\rm crit}(\mathcal{M}_1) - L_\nu^{\rm crit}(\mathcal{M}_2)|/L_\nu^{\rm crit}(\mathcal{M}_1)$, at each $\dot{M}$ when $\mathcal{M}$ is increased as $1.3 \rightarrow 2.0$ and $2.0 \rightarrow 3.0$. The "data" rows use simulation data for $L_\nu^{\rm crit}$ with fiducial inputs. The "eqn." rows use output from Equation (22), where we use $L_\nu^{\rm crit}$ data at $\dot{M} = 0.5\,M_\odot$ s^{-1} for each $\mathcal{M}$ to scale Equation (22).

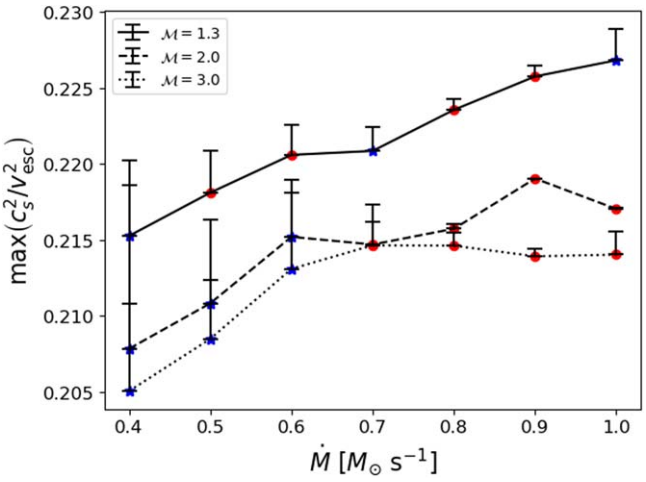

Figure 9. Maximum antesonic ratio for stable models with fiducial inputs at $L_\nu^{\rm crit,n}$ using $\mathcal{M} = 1.3$ (solid line), $\mathcal{M} = 2.0$ (dashed line), and $\mathcal{M} = 3.0$ (dotted line). Blue stars represent oscillatory stable models, which use the time-averaged value of the maximum antesonic ratio. Red dots represent nonoscillatory stable models, which use the maximum antesonic ratio once steady state is reached. The bars indicate the maximum value achieved over all t during each simulation.

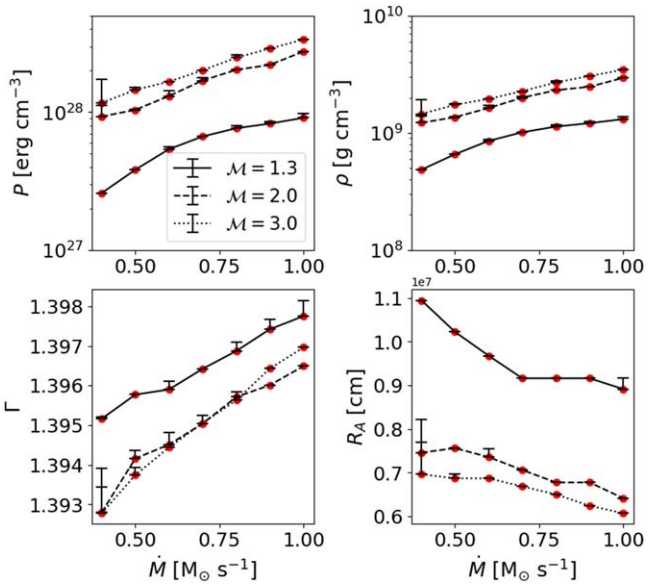

Figure 10. Antesonic ratio quantities (Equation (27)), i.e., P, ρ, Γ, and R_A for near-critical fiducial models with $\mathcal{M} = 1.3$ (solid), $\mathcal{M} = 2.0$ (dashed), and $\mathcal{M} = 3.0$ (dotted) plotted over $\dot{M}$. As in Figure 9, the bars here indicate maximum values achieved during the simulation. The red dots are the representative values for each model, thus they are either the time-averaged value (for stable oscillatory models) or the final time value (for stable nonoscillatory models).

shows the relevant antesonic ratio quantities in the nonrelativistic limit evaluated at the maximum antesonic ratio radius R_A,

$$\max\left(\frac{c_s^2}{v_{\rm esc}^2}\right) \simeq \frac{R_A}{2GM}\frac{\Gamma P}{\rho}, \tag{27}$$

where their maxima in time are indicated by bars. P, ρ, and Γ increase with $\dot{M}$ (and $L_\nu^{\rm crit,n}$), while R_A decreases. Note that P and ρ increase while Γ and R_A decrease with $\mathcal{M}$, but all values begin converging for $\mathcal{M} \gtrsim 2.0$. The time-dependent changes in these quantities manifest as the changes shown in Figure 9.

When L_ν increases at fixed $\dot{M}$, ρ increases more quickly than ΓP. As a result, c_s is driven to smaller values and approaches a minimum at $L_\nu^{\rm crit,n}$ (see top panel of Figure 11) The bottom panel of Figure 11 shows the time-averaged antesonic ratio as a function of r over a range of L_ν at fixed $\dot{M}$. The maximum ratio, indicated by red dots, increases with L_ν. Because R_A increases with L_ν at fixed $\dot{M}$, this causes $v_{\rm esc}(R_A)$ to decrease (top panel of Figure 11). However, $v_{\rm esc}(R_A)$ decreases more rapidly with L_ν than $c_s(R_A)$, so the ratio $c_s^2/v_{\rm esc}^2$ increases with higher L_ν. Because $L_\nu^{\rm crit}$ increases with $\dot{M}$, stable models at higher $\dot{M}$ have wider ranges of c_s and $v_{\rm esc}$ values, which yields higher critical antesonic ratios. This is shown in Figure 9, where the maximum antesonic ratio generally increases with $L_\nu^{\rm crit,n}$ for $\mathcal{M} = 1.3$ and 2.0. For $\mathcal{M} = 3.0$, the ratio increases with $\dot{M}$ for $\dot{M} \lesssim 0.6\,M_\odot$ s^{-1} but is roughly constant for greater $\dot{M}$ and exhibits the expected behavior for near-pressureless freefall (O. Pejcha & T. A. Thompson 2012).

The ratio decreases with higher $\mathcal{M}$ for most models and begins converging after $\mathcal{M} \gtrsim 2.0$ (see Figure 9), e.g., it decreases by an average of $\sim$4% for $\mathcal{M} = 1.3 \rightarrow 2.0$ and $\sim$1% for $\mathcal{M} = 2.0 \rightarrow 3.0$. When the pre-shock P drops ($\mathcal{M}$ is increased), $P_{\rm ram}$ at the shock increases (see Figure 1). This drives $R_{\rm shock}$ and $R_{\rm gain}$ to lower radii. Lower P leads to a subtle steepening of the post-shock T gradient. Because $\dot{Q}_C$ sensitively depends on T, this subtle change in T allows $\dot{Q}_H$ to dominate $\dot{Q}_C$ at lower radii, thus leading to smaller $R_{\rm gain}$. As a result, $v_{\rm esc} \propto 1/\sqrt{R_A}$ increases with $\mathcal{M}$, where $R_A \sim R_{\rm gain}$ for nonisothermal models (O. Pejcha & T. A. Thompson 2012; M. J. Raives et al. 2021). Near $R_{\rm gain}$, c_s also increases with $\mathcal{M}$. However, the absolute change in $v_{\rm esc}$ with respect to $\mathcal{M}$ is greater than the absolute change in c_s. This is what drives the near-critical antesonic ratio down in value for higher $\mathcal{M}$.

The fiducial model set in O. Pejcha & T. A. Thompson (2012) predicts a near-constant maximum antesonic ratio along the critical curve. We find that, for a given set of inputs, there is

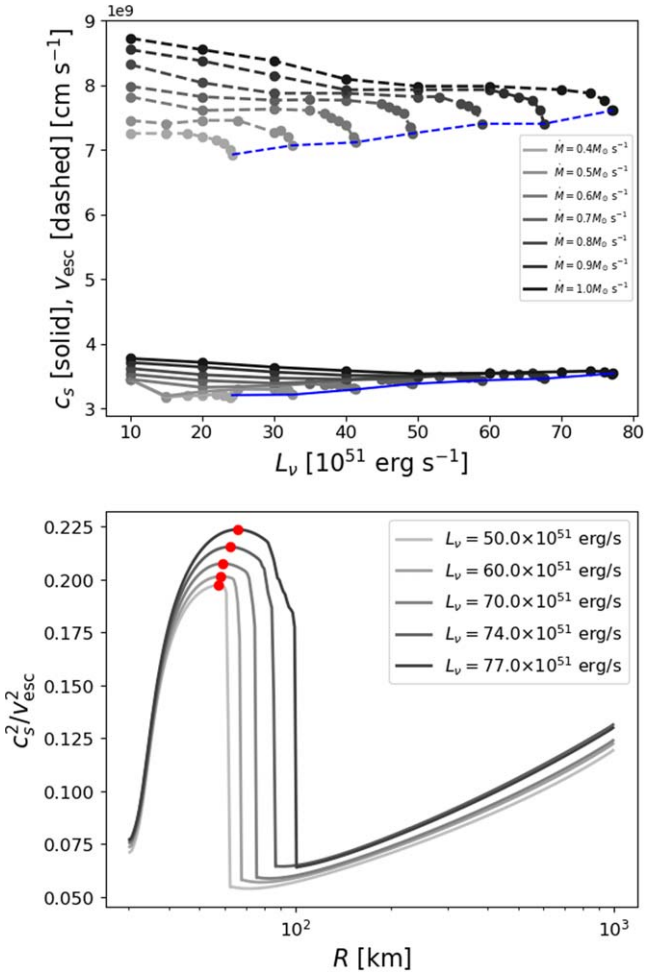

Figure 11. Top: time-averaged c_s and v_{esc} as functions of L_ν and $\dot{M}$ evaluated at R_A for $\mathcal{M} = 2.0$. The dots show the evolution of c_s and v_{esc} with L_ν at fixed $\dot{M}$, where c_s and v_{esc} decrease in value and reach a minimum near the critical luminosity. As $\dot{M}$ is increased, this minimum is increased for both quantities, as illustrated by a solid blue line for c_s and a dashed blue line for v_{esc}. Bottom: time-averaged antesonic ratio for stable models beneath L_ν^{crit} at $\dot{M} = 1.0\,M_\odot$ s^{-1} and $\mathcal{M} = 2.0$. The maximum of the ratio (red dot), which occurs around R_{gain}, increases and is pushed to larger radii as criticality is neared.

always a critical value above which the flow transitions from accretion to explosion. However, while the changes across the range of $\dot{M}$ we explore are small, the critical antesonic ratio is not constant for low $\mathcal{M}$ and is a function of the inputs, e.g., $\dot{M}$, $\mathcal{M}$, and L_ν, as shown in Figure 9. We find that pressurized preshock inflow modifies the antesonic condition, which is not captured by semi-analytic models that use $P = 0$ as a boundary condition ahead of the shock. We also observe time-dependent dynamics that temporarily boost the maximum antesonic ratio (Figures 9 and 10). Shock oscillations and pressurized freefall are not accounted for in the models created by O. Pejcha & T. A. Thompson (2012), therefore their models do not capture the full variation of c_s^2/v_{esc}^2 along the critical curve. Nonetheless, the high-$\dot{M}$ and high-$\mathcal{M}$ models shown in Figure 9 are remarkably consistent with the constant antesonic ratio determined by O. Pejcha & T. A. Thompson (2012).

3.4. Advection and Heating Timescales

If the timescale for a fluid parcel to advect through the gain region τ_{adv} is longer than the timescale for the gain region to be sufficiently heated via neutrino–matter interactions τ_{heat}, then the internal energy of the fluid inside the gain region will increase before the fluid accretes below R_{gain}. This energy may be delivered to the shock and lead to an explosion, and thus the comparison between these two timescales might provide a quantitative explosion condition (C. Thompson 2000; T. A. Thompson et al. 2005; J. W. Murphy & A. Burrows 2008). Various definitions of the advection and heating timescales may be considered, which may lead to better quantitative descriptions of the critical luminosity. For example, the advection timescale may be defined as the time required for fluid to flow through a pressure scale height H (e.g., T. A. Thompson et al. 2005):

$$\tau_{adv,1}(r) = \left|\frac{H}{v_r}\right| = \left|\frac{\left(\frac{d\ln P}{dr}\right)^{-1}}{v_r}\right|, \tag{28}$$

and the heating timescale may be defined as

$$\tau_{heat,1}(r) = \left|\frac{\epsilon}{\rho}\frac{1}{\dot{Q}}\right| \sim \left|\frac{P}{\rho}\frac{1}{\dot{Q}}\right|, \tag{29}$$

where $\dot{Q}$ is the net heating rate. Alternatively, the definition for the advection timescale could be formulated in terms of an integral, to capture the total time in the gain region (J. W. Murphy & A. Burrows 2008):

$$\tau_{adv,2}(t) = \int_{R_{gain}}^{R_{shock}} \frac{dr}{|v_r|}. \tag{30}$$

Similarly, one could define the heating timescale in spherical symmetry in terms of the ratio of the total internal energy in the gain region to the total net heating rate in the gain region (J. W. Murphy & A. Burrows 2008; O. Pejcha & T. A. Thompson 2012; J. W. Murphy & J. C. Dolence 2017):

$$\tau_{heat,2}(t) = \frac{\int_{R_{gain}}^{R_{shock}} dr\, r^2\, \rho\, \epsilon}{\int_{R_{gain}}^{R_{shock}} dr\, r^2\, \rho\, \dot{Q}}. \tag{31}$$

In these cases, one might expect the critical condition for explosion to be set by τ_{adv}/τ_{heat} such that for

$$\frac{\tau_{adv}}{\tau_{heat}} > 1, \tag{32}$$

an explosion may soon follow.

To test these timescale criteria, we evaluate $\max(\tau_{adv,1}/\tau_{heat,1})$ and $\max(\tau_{adv,2}/\tau_{heat,2})$ (see Figure 12) at $L_\nu^{crit,n}$. Note that we compute $\tau_{adv,1}$ and $\tau_{heat,1}$ with time-averaged quantities, then we find $\max(\tau_{adv,1}/\tau_{heat,1})$ within the gain region. To understand how $\max(\tau_{adv,1}/\tau_{heat,1})$ changes with $\mathcal{M}$, we consider the constituent terms in Equations (28) and (29). R_{gain} and R_{shock} decrease when $\mathcal{M}$ increases. As a result, the maximum timescale ratio is driven to smaller radii, i.e., regions with higher P and $\epsilon.\dot{Q}$ in the gain region grows with larger $\mathcal{M}$, which contributes to lowering the timescale ratio. However, the changes in P, r, and ϵ overpower the changes in $\dot{Q}$ at the radius where the timescale ratio maximizes, and they all directly contribute to the growth of $\max(\tau_{adv,1}/\tau_{heat,1})$ with $\mathcal{M}$. Similarly to the antesonic ratio and L_ν^{crit}, $\max(\tau_{adv,1}/\tau_{heat,1})$ converges as a function of $\mathcal{M}$ after $\mathcal{M} \gtrsim 2.0$ (see Figure 12), e.g., the ratio increases by ∼42% for $\mathcal{M} = 1.3 \rightarrow 2.0$ and ∼10% for $\mathcal{M} = 2.0 \rightarrow 3.0$. Otherwise,

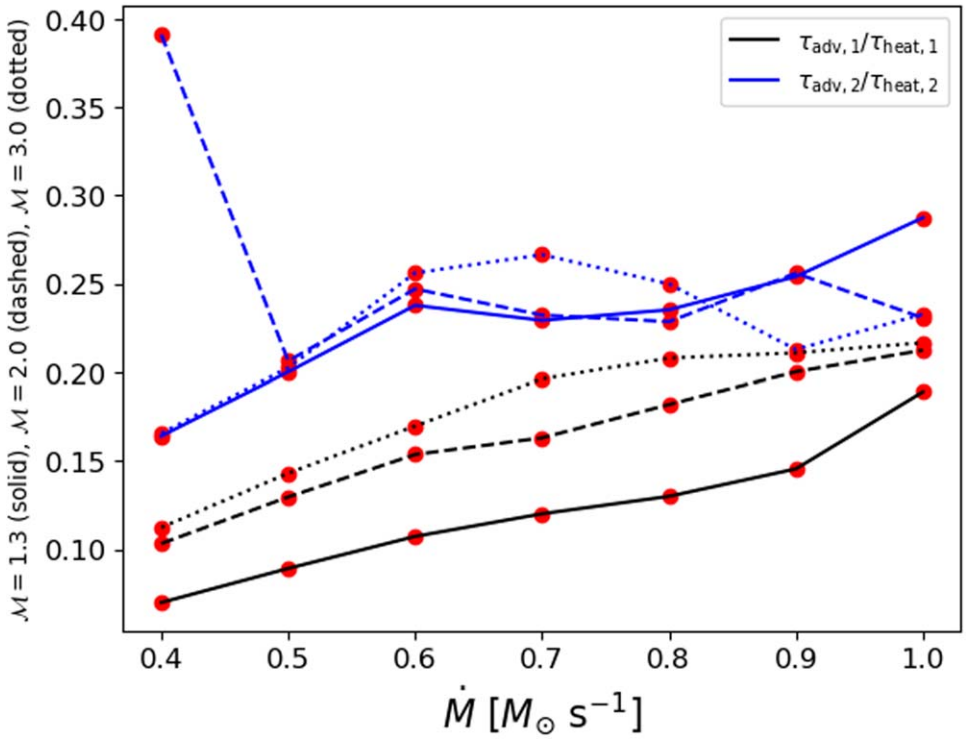

Figure 12. Maximum advection and heating timescale ratios for $\mathcal{M} = 1.3$ (solid), $\mathcal{M} = 2.0$ (dashed), and $\mathcal{M} = 3.0$ (dotted) for fiducial near-critical stable models. The black profile is calculated with Equations (28) and (29), and the blue profile is calculated with Equations (30). The ratios remain below unity until a model begins exploding. The black profiles demonstrate $\mathcal{M}$ dependence.

$\max(\tau_{\rm adv,1}/\tau_{\rm heat,1})$ increases by a factor of two to three along $L_\nu^{\rm crit,n}$ depending on $\mathcal{M}$.

Excluding the data point at $\dot{M} = 0.4\,M_\odot$ s^{-1} and $\mathcal{M} = 2.0$, we find that $\max(\tau_{\rm adv,2}/\tau_{\rm heat,2})$ increases by a factor of 0.5–0.7 depending on $\mathcal{M}$. This is due to the changes in the post-shock ρ in response to $\dot{M}$ and L_ν, which incurs changes in $M_{\rm gain}$ that directly map into the maximum timescale ratio (see Figure 13). This timescale ratio does not have a strong dependence on $\mathcal{M}$ compared to $\max(\tau_{\rm adv,1}/\tau_{\rm heat,1})$. In contrast to the results in O. Pejcha & T. A. Thompson (2012), we find that $\max(\tau_{\rm adv,2}/\tau_{\rm heat,2})$ does not monotonically increase with $L_\nu^{\rm crit,n}$ (see Figure 12).

Our subcritical models maintain $\tau_{\rm adv}/\tau_{\rm heat} < 1$. Some models, e.g., the model with $\mathcal{M} = 2.0$ and $\dot{M} = 0.4\,M_\odot$ s^{-1} in Figure 12, may have larger timescale values than others due to shock oscillations, which extends the gain region and may increase the value of $M_{\rm gain}$ or alter the post-shock P, ϵ, and $\dot{Q}$ values. Otherwise, the timescale ratio for near-critical models is similar to the 1D values obtained by J. W. Murphy & A. Burrows (2008). We confirm that $\tau_{\rm adv}/\tau_{\rm heat}$ exceeds unity after the explosion sets in. This is demonstrated in Figure 14, which shows the time evolution of $\tau_{\rm adv,2}/\tau_{\rm heat,2}$ for models with successively higher L_ν.

3.5. Force Explosion Condition

J. W. Murphy & J. C. Dolence (2017), M. Gogilashvili & J. W. Murphy (2022), and M. Gogilashvili et al. (2023) have shown that, by integrating the equations for fluid dynamics, they arrive at an expression that computes the net forces acting on the shock. Using this, they show that all models above the critical curve proposed in A. Burrows & J. Goshy (1993) have a force imbalance for which no stable solutions exist and $V_{\rm shock}$ must be positive. To derive this condition, J. W. Murphy & J. C. Dolence (2017) and M. Gogilashvili & J. W. Murphy (2022) integrate in volume the momentum equation (Equation (2)) for time-independent, spherically symmetric accretion flow, which leads to an equation for the net forces acting on the shock. The sum of these forces gives the integral FEC Ψ:

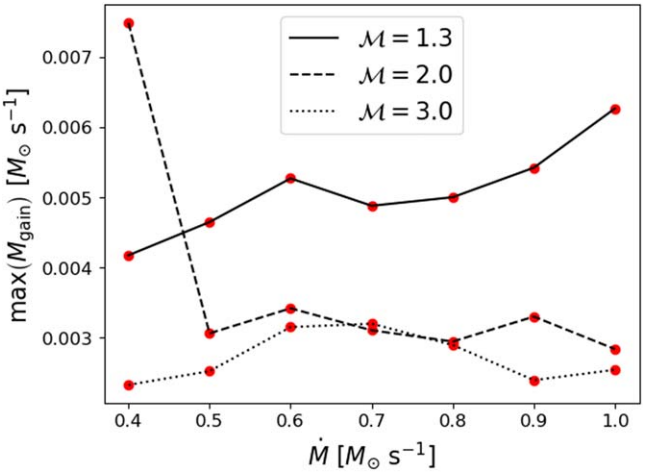

Figure 13. Maximum mass enclosed in the gain region $M_{\rm gain}$ for fiducial near-critical models. The behavior in $M_{\rm gain}$ profiles directly corresponds to the maximum timescale ratios with $\tau_{\rm adv,2}$ (see Figure 12). At $\dot{M} = 0.4\,M_\odot$ s^{-1}, the $\mathcal{M} = 2.0$ curve is driven up by shock oscillations.

$$\Psi = (P_\star + \rho_\star v_{r,\star}^2)R_\star^2 - (P_{s+} + \rho_{s+} v_{r,s+}^2)R_s^2 + \int_{R_\star}^{R_s} 2Pr\,dr - GM_\star \int_{R_\star}^{R_s} \rho\,dr, \quad (33)$$

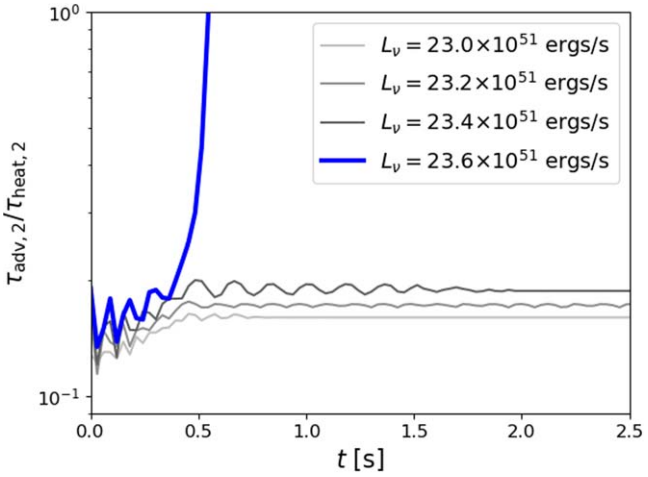

Figure 14. Advection and heating timescale ratio for Equations (30) and (31) plotted over t for fiducial models with $\dot{M} = 0.5\,M_\odot\ \mathrm{s}^{-1}$ and $\mathcal{M} = 1.3$. Models with $L_\nu < 23.6 \times 10^{51}\ \mathrm{erg\ s}^{-1}$ are stable, whereas $L_\nu^{\mathrm{crit}} = 23.6 \times 10^{51}\ \mathrm{erg\ s}^{-1}$ (blue line) explodes. At L_ν^{crit}, the calculation stops once the shock reaches the outer boundary and the ratio exceeds unity. Oscillations in the profiles are due to oscillations in the shock as criticality is approached. Note that $\max(\tau_{\mathrm{adv},1}/\tau_{\mathrm{heat},1})$ demonstrates similar behavior.

where "$s+$" indicates the region just above the shock. Equation (33) computes the net forces on the shock due to P_{ram}, the pressure gradient, and gravity. The FEC is typically evaluated in the dimensionless form $\tilde{\Psi}$ (M. Gogilashvili & J. W. Murphy 2022),

$$\tilde{\Psi} = \frac{\Psi}{\dot{M}_{1.0}\sqrt{\frac{GM_\star}{R_\star}}\ \mathrm{M}_\odot\ \mathrm{s}^{-1}}, \tag{34}$$

where we choose to normalize Ψ by $\dot{M}_{1.0} = \dot{M}/1.0\,M_\odot\ \mathrm{s}^{-1}$. J. W. Murphy & J. C. Dolence (2017) and M. Gogilashvili & J. W. Murphy (2022) show that one can evaluate $\tilde{\Psi}$ as a function of $x_{\mathrm{shock}} = R_{\mathrm{shock}}/R_\star$ by solving the time-independent Euler equations with the strong shock jump conditions. If $\min(\tilde{\Psi}(x_{\mathrm{shock}})) < 0$, then $\tilde{\Psi}(x_{\mathrm{shock}})$ crosses an equilibrium state where $V_{\mathrm{shock}} = 0$. In this case, $\tilde{\Psi} > 0$ or $\tilde{\Psi} < 0$ corresponds to either $V_{\mathrm{shock}} > 0$ or $V_{\mathrm{shock}} < 0$, respectively, which indicates that the shock may be forced toward the equilibrium state. Otherwise, if $\min(\tilde{\Psi}(x_{\mathrm{shock}})) > 0$, then $V_{\mathrm{shock}} > 0$ for all x_{shock}, and no stable solution exists. Further, J. W. Murphy & J. C. Dolence (2017) performed this analysis by using inputs from their numerical models at each time step to determine $\min(\tilde{\Psi}(x_{\mathrm{shock}}))$, which showed how close their accretion models were to exploding at each moment, i.e., a "nearness-to-explosion" condition. Alternatively, a fully analytic FEC can be derived from $\min(\tilde{\Psi}) = 0$, which has been shown to accurately predict explosions for numerical simulations (M. Gogilashvili & J. W. Murphy 2022; M. Gogilashvili et al. 2023).

To assess the FEC, we compute $\tilde{\Psi}$ directly from Equation (34) using simulation data. If $\tilde{\Psi}(t) \sim 0$, this indicates that the shock is stable. Otherwise, $\tilde{\Psi}(t) > 0$ indicates an explosion. Unlike the nearness-to-explosion condition, this procedure does not indicate how close a model is to exploding because $\tilde{\Psi}(t)$ is not necessarily being evaluated at its minimum with respect to R_{shock}. However, it can still be used to identify

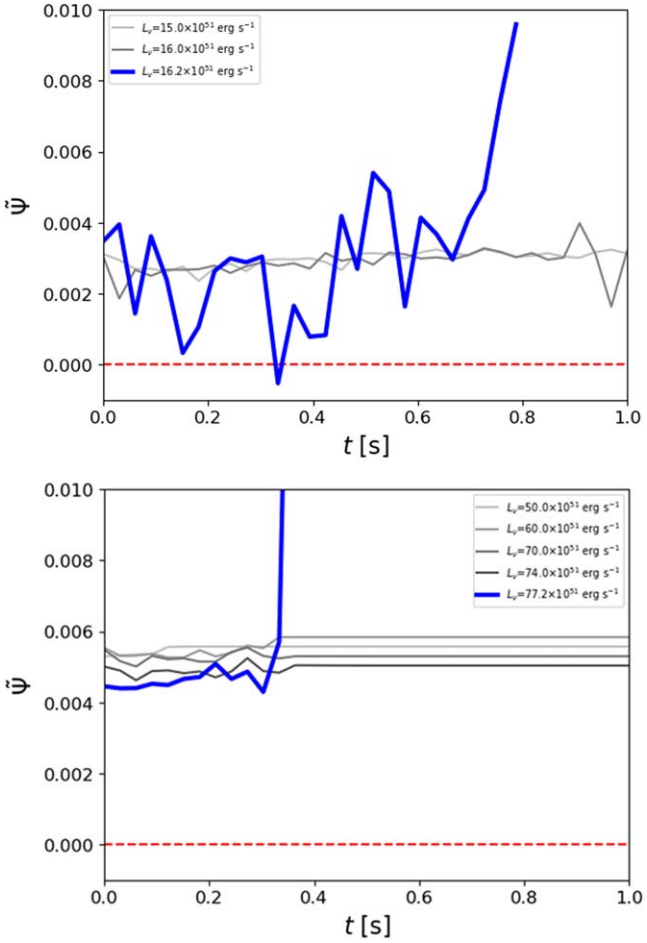

Figure 15. $\tilde{\Psi}$ as a function of time. (Top) $\tilde{\Psi}$ for a series of models at $\dot{M} = 0.3\,M_\odot\ \mathrm{s}^{-1}$ and $\mathcal{M} = 2.0$ with fiducial inputs. $\tilde{\Psi}$ oscillates around 3.0×10^{-3} for stable models. At $L_\nu^{\mathrm{crit}} = 16.2 \times 10^{51}\ \mathrm{erg\ s}^{-1}$ (blue), $\tilde{\Psi}$ is driven up in value. The red dashed line at $\tilde{\Psi} = 0$ shows the expected value of $\tilde{\Psi}$ for nonoscillatory stable models. (Bottom) Same configuration as the top panel, but for models at $\dot{M} = 1.0\,M_\odot\ \mathrm{s}^{-1}$ with $L_\nu^{\mathrm{crit}} = 77.2 \times 10^{51}\ \mathrm{erg\ s}^{-1}$. All subcritical models here become time-steady for $t > 0.35$ s.

an explosion once it occurs (J. W. Murphy & J. C. Dolence 2017). Figure 15 shows the time evolution of $\tilde{\Psi}$ for several stable models and an exploding model (blue). On average, we find positive values of $\tilde{\Psi}$ for stable models, but we also find that shock oscillations can briefly drive $\tilde{\Psi}$ down to negative values (top panel of Figure 15). Once L_ν^{crit} is exceeded and the shock moves out, $\tilde{\Psi}$ rapidly increases. In this manner, Equation (34) operates similarly to tracking R_{shock} in time (J. W. Murphy & J. C. Dolence 2017).

In Figure 16, we show summary results along the critical curve. Similarly to J. W. Murphy & J. C. Dolence (2017), we find that $\tilde{\Psi} \gtrsim 0$ for near-critical models. Especially at low $\dot{M}$, time-dependent fluctuations may drive $\tilde{\Psi}$ above and below zero (Figure 16). We also find that $\tilde{\Psi}$ increases by a factor of $\simeq$0.2–2 along $L_\nu^{\mathrm{crit,n}}$, depending on $\mathcal{M}$. This behavior is linked to the properties of the post-shock structure. More matter accretes through the shock at higher $\dot{M}$, which increases the post-shock thermal content and densities. The integrated pressure and density terms in Equation (33) increase with $\dot{M}$ in response to these changes in the post-shock flow, but the relative difference between these terms decreases with $\dot{M}$. This causes $\tilde{\Psi}$ to

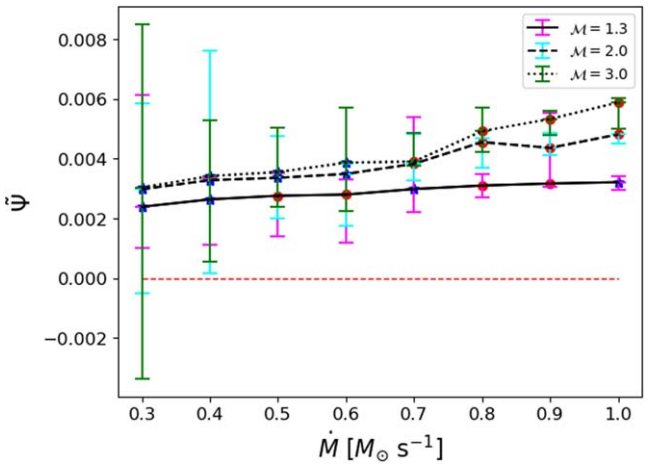

Figure 16. $\tilde{\Psi}$ for near-critical models with fiducial inputs as a function of $\dot{M}$ at $\mathcal{M} = 1.3$ (solid, magenta cap), $\mathcal{M} = 2.0$ (dashed, cyan cap), and $\mathcal{M} = 3.0$ (dotted, green cap). Blue stars indicate oscillatory stable models, which use the time-averaged value of $\tilde{\Psi}$. Red dots indicate nonoscillatory stable models, which use the value of $\tilde{\Psi}$ at the final time step. The bars indicate the minimum and maximum variation of $\tilde{\Psi}$ in time. Stable models should have $\tilde{\Psi} = 0$, but we find $\tilde{\Psi}$ to generally be slightly positive.

increase along $\dot{M}$ for near-critical models. Note that, in Equation (33), the pre-shock quantities are approximately an order of magnitude less than all the other terms, and thus their responses to changes in $\dot{M}$ are negligible. Meanwhile, the quantities located at $R_\star$ are approximately constant for all $\dot{M}$.

$\tilde{\Psi}$ depends on $\mathcal{M}$ (Figure 16), but converges as $\mathcal{M}$ is increased. We observe an average change of $\sim$24% in $\tilde{\Psi}$ when $\mathcal{M} = 1.3 \rightarrow 2.0$ and $\sim$8% when $\mathcal{M} = 2.0 \rightarrow 3.0$. As shown in Figure 1, changing $\mathcal{M}$ modifies the position of $R_{\rm shock}$, which maps to Equation (33) through the limits of integration. When $R_{\rm shock}$ is driven to smaller radii through $\mathcal{M}$, both integrated quantities in Equation (33) decrease. Because the integral over $GM_\star\rho$ dominates in $\tilde{\Psi}$, the overall value of $\tilde{\Psi}$ increases when the integrand $GM_\star\rho$ decreases. As such, $\tilde{\Psi}$ depends on $\mathcal{M}$ primarily through $R_{\rm shock}$.

3.6. Implications of $\mathcal{M}$ for Realistic Progenitors

Previous work implies a direct connection between the accretion of compositional interfaces and the initiation of explosion (J. W. Murphy & A. Burrows 2008; F. Hanke et al. 2013; Y. Suwa et al. 2015; C. D. Ott et al. 2018; A. Summa et al. 2018; D. Vartanyan et al. 2018; T. Wang et al. 2022; A. Burrows et al. 2024). L. Boccioli et al. (2025) even connect the FEC to the onset of explosion due to the accretion of compositional interfaces, which supports the validity of explosion conditions and their ties to progenitor structure. Specifically, the rapid decrease in density across the Si/O interface is important for explosion, because once it accretes onto the stalled accretion shock, it causes a decrease in both $\dot{M}$ and $P_{\rm ram}$ (D. Vartanyan et al. 2018; T. Wang et al. 2022).

In the context of the critical curve, it is natural to associate a decrease in $\dot{M}$ at approximately fixed L_ν as the condition needed to cross the critical threshold for explosion (e.g., Figures 6 and 7). Here, we briefly assess whether the change in the thermal content across the compositional boundaries in realistic progenitors might substantively affect $L_\nu^{\rm crit}$, independent of $\dot{M}$, as suggested by our results in Figure 7.

In Sections 3–3.5, we use $\bar{A} = 1$ globally to simplify our model and focus on the changes in $L_\nu^{\rm crit}$ with respect to $\mathcal{M}$. In this section, we make direct comparisons between our models and realistic progenitors by setting $\bar{A} = 56$ (for Fe nuclei) between the shock and the outer boundary and $\bar{A} = 1$ (for free nucleons) for $r < R_{\rm shock}$. This changes the mapping between $\mathcal{M}$ and S at the outer boundary and is more realistic than globally setting $\bar{A} = 1$. We specify an electron fraction $Y_{e,\rm out} = 26/56$, a mass-accretion rate $\dot{M}_{\rm out}$, and an entropy $S_{\rm out}$ at the outer boundary. We then specify the fraction of escape velocity $\mathcal{F} = 0.8$ at which the material is accreting at the outer boundary, i.e., $v_{r,\rm out} = \mathcal{F} v_{\rm esc,out}$. By using these outer boundary parameters with the EoS and $\rho_{\rm out} = \dot{M}_{\rm out}/4\pi\, R_{\rm out}^2 v_{r,\rm out}$, the thermal state at $R_{\rm out}$ is fully determined.

The top panel of Figure 17 shows the mapping between the mass coordinate M and entropy S for realistic massive progenitors (T. Sukhbold et al. 2016), where dots mark the Si/O interfaces. For these data, $\dot{M}$ near the outer edge of the iron core (indicated by crosses) is on the order of $1\,M_\odot\ \mathrm{s}^{-1}$ (indicated by right arrows) and decreases to $\sim 0.1\,M_\odot\ \mathrm{s}^{-1}$ generally within or near the Si layer. For reference, we mark $\dot{M} = 0.3\,M_\odot\ \mathrm{s}^{-1}$ with left arrows to indicate the minimum $\dot{M}$ we explored in previous sections. For the study in this section, we select $\dot{M} = 0.7\,M_\odot\ \mathrm{s}^{-1}$ as a representative mass-accretion rate at the outer boundary that fits within this range. The entropies with this range of $\dot{M}$ are $S \sim 1 \rightarrow 3\,k_{\rm B}\ \mathrm{baryon}^{-1}$, whereas entropies in the O layer are near $\sim 6 \rightarrow 7\,k_{\rm B}\ \mathrm{baryon}^{-1}$. This guides our choice for $S_{\rm out}$. Note that, with $\bar{A} = 56$, the lower entropy range corresponds to a higher $\mathcal{M}$ value than those we studied in previous sections (see bottom panel of Figure 17).

The middle panel in Figure 17 shows how $L_\nu^{\rm crit}$ depends on $S_{\rm out}$ at fixed $\dot{M}$ with this new boundary condition. $S_{\rm out}$ is selected between a range of $1 \rightarrow 7\,k_{\rm B}\ \mathrm{baryon}^{-1}$ to fully capture the relevant thermal content for all progenitor data discussed here. For the total progenitor mass M_T data of $M_T = 9.75\,M_\odot$, $15\,M_\odot$, and $25\,M_\odot$, we observe a gradual increase in entropy of $S \sim 1.1 \rightarrow 1.9\,k_{\rm B}\ \mathrm{baryon}^{-1}$, $S \sim 1.7 \rightarrow 2.7\,k_{\rm B}\ \mathrm{baryon}^{-1}$, and $S \sim 1.5 \rightarrow 3.0\,k_{\rm B}\ \mathrm{baryon}^{-1}$, respectively, within a mass-accretion rate range of $0.3\,M_\odot\ \mathrm{s}^{-1} \leqslant \dot{M} \leqslant 1.0\,M_\odot\ \mathrm{s}^{-1}$ (see Figure 17). For the aforementioned models, we find that these changes in entropy alone (neglecting the effects of $\dot{M}$) correspond to fractional decreases in $L_\nu^{\rm crit}$ by approximately 4%, 5%, and 8%, respectively. Note that these decreases are at most on the order of the results shown in Table 1 ($\sim$10%). Because $\dot{M} = 0.7\,M_\odot\ \mathrm{s}^{-1}$ for all $L_\nu^{\rm crit}$ shown in Figure 17, the results here indicate that, at the stalled shock, the accretion of material in a progenitor with gradually increasing S affects $L_\nu^{\rm crit}$ independently of $\dot{M}$.

In Figure 17, we explore higher entropy ranges ($3\,k_{\rm B}\ \mathrm{baryon}^{-1} \lesssim S \lesssim 7\,k_{\rm B}\ \mathrm{baryon}^{-1}$) to illustrate the potential behavior of $L_\nu^{\rm crit}$ due to thermal content changes when the Si/O layer accretes onto the shock. In this case, we estimate the fractional decrease in $L_\nu^{\rm crit}$ to be on the order of $\sim$10% for all models shown here. However, the value of $\dot{M}$ for these progenitor data at the Si/O layer and beyond drops below our tested range, and thus a more complete investigation of how $L_\nu^{\rm crit}$ depends on S and $\mathcal{M}$ for $\dot{M} < 0.3\,M_\odot\ \mathrm{s}^{-1}$ is warranted.

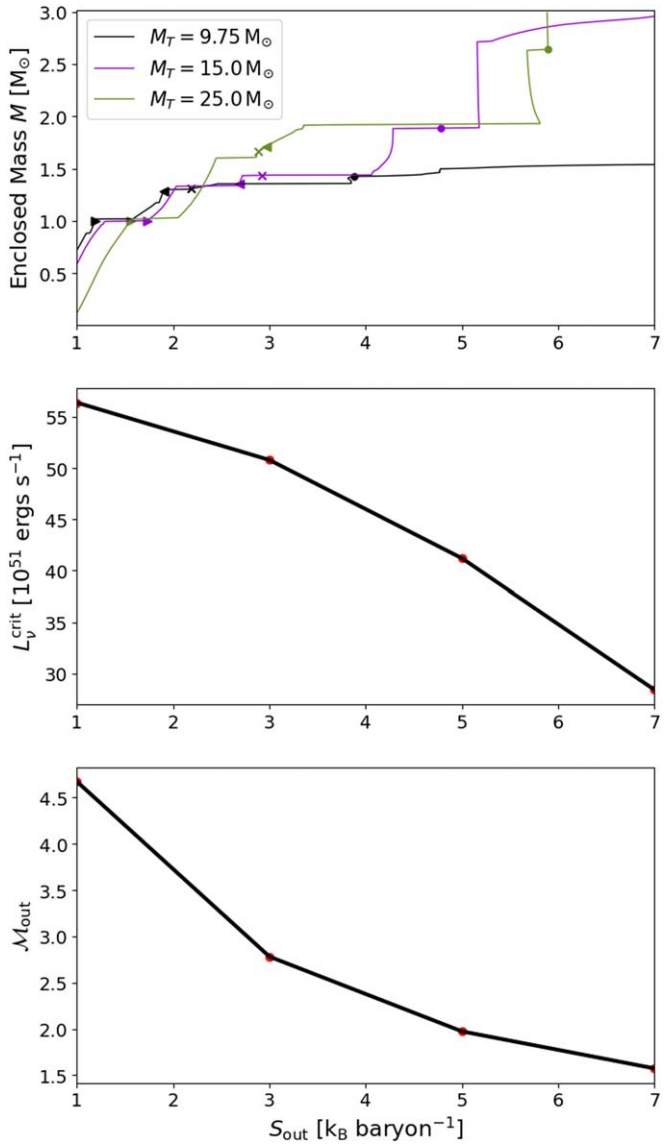

Figure 17. Top: enclosed-mass M profiles as functions of S for pre-collapse solar-metallicity progenitors of total masses $M_T = 9.75\,M_\odot$ (black), $M_T = 15\,M_\odot$ (violet), and $M_T = 25\,M_\odot$ (green) from the T. Sukhbold et al. (2018) progenitor data set. The discontinuities ($dM/dS \to \infty$) in the profiles correspond roughly to compositional layers, i.e., regions of constant entropy, whereas the flat regions ($dM/dS \sim 0$) indicate the boundaries between the layers. The dots indicate the Si/O boundaries, the crosses indicate the edges of the iron cores, and the right (left) arrows indicate the regions of maximum (minimum) $\dot{M}$ explored in this work. Middle: $L_\nu^{\rm crit}$ as a function of $S_{\rm out}$ for models with $\dot{M} = 0.7\,M_\odot\,{\rm s}^{-1}$, fiducial $R_\star$, $M_\star$, and $\langle\epsilon_{\nu_e}\rangle$ that use the $\bar{A}$ treatment and boundary condition specified in Section 3.6. Bottom: outer boundary Mach number $\mathcal{M}_{\rm out}$ as a function of $S_{\rm out}$ for the same data from the middle panel.

4. Conclusions

Using Athena++, we have constructed core-collapse supernova accretion models in time-dependent spherical symmetry with a general EoS and optically thin neutrino heating and cooling, to more fully understand the critical neutrino luminosity $L_\nu^{\rm crit}$ and to analyze the explosion conditions, e.g., the antesonic condition, the heuristic timescale condition, and the FEC. Our input parameters include the neutrino luminosity L_ν, average neutrino energy $\langle\epsilon_\nu\rangle$, accretion rate $\dot{M}$, Mach number of the accreted material $\mathcal{M}$, PNS radius $R_\star$, mass $M_\star$, and neutrino optical depth τ. We use L_ν and $\dot{M}$ to map the critical curve, and we study the explosion conditions (Sections 3.3, 3.4, and 3.5) using the steady accretion solutions nearest to explosion $L_\nu^{\rm crit,n}$. We evolve models up to $t = 3$ s to achieve nonoscillatory stability (predominantly at high $\dot{M}$), oscillatory stability (predominantly at low $\dot{M}$), or explosion. We summarize our findings as follows:

1. Similarly to past studies, we quantify how the critical neutrino luminosity $L_\nu^{\rm crit}$ for explosion depends on the key parameters of the problem, including the PNS radius, mass, and the average neutrino energy (see Section 3.2.1 and Figure 6). In particular, we find the numerical results $L_\nu^{\rm crit} \propto R_\star^{-2.58}$, $L_\nu^{\rm crit} \propto M_\star^{1.97}$, $L_\nu^{\rm crit} \propto \langle\epsilon_{\nu_e}\rangle^{-1.69}$, and $L_\nu^{\rm crit} \propto \dot{M}^{1.29}$. We generally find time-dependent oscillatory solutions at low $\dot{M}$ and time-steady nonoscillatory accretion at high $\dot{M}$ (see D. Gabay et al. 2015).
2. Differing from previous works, we study the dependence of $L_\nu^{\rm crit}$ on the thermal content of the accreted matter, as parameterized by the gas Mach number ($\mathcal{M}$) at the outer edge of our computational domain. Higher $\mathcal{M}$ corresponds to lower thermal content, which drives the pre-shock flow closer to the limit of pressureless freefall. Importantly, we show that $L_\nu^{\rm crit}$ decreases as the thermal content of the accreted material increases (whereas $\mathcal{M}$ decreases; see Section 3.2.1). For fixed $\dot{M}$, lower $\mathcal{M}$ decreases the ram pressure at the shock (see Figure 1), leading to lower $L_\nu^{\rm crit}$ for explosion. As expected, the value of $L_\nu^{\rm crit}$ converges as $\mathcal{M}$ increases, because the system approaches the limit of pressureless freefall (high $\mathcal{M}$; see Figure 7).
3. We assess the importance of the thermal content of the accreted material—as parameterized by $\mathcal{M}$ and S—for realistic progenitors in Section 3.6. In Figure 17, we show that the normalization of $L_\nu^{\rm crit}$ at fixed $\dot{M}$ decreases by ∼5%–8% as the entropy of the accreted material increases from ∼1 to $3\,k_{\rm B}$ baryon^{-1}. Accretion of the Si/O boundary, which corresponds to a larger increase in entropy, may cause an even greater fractional decrease in $L_\nu^{\rm crit}$ ($\gtrsim$10%), but further investigation is required to determine the effects of the pre-shock thermal content on $L_\nu^{\rm crit}$ for the low values of $\dot{M} < 0.3\,M_\odot\,{\rm s}^{-1}$ that correspond to the accretion of those layers.
4. We assess several critical conditions for explosion that have been suggested in the literature, including the so-called "antesonic" condition (see Section 3.3). We find a nearly constant critical antesonic ratio of $\max(c_s^2/v_{\rm esc}^2) \simeq 0.215 \pm 0.01$ in the post-shock medium, but with dependencies on $\mathcal{M}$ and $\dot{M}$. The maximum critical antesonic ratio changes by ≃3%–5%, depending on $\mathcal{M}$, across the range of $\dot{M}$ we explore (Figure 9). Pressurized inflow and time-dependent dynamics modify the behavior of the antesonic ratio in a way that is not captured by semi-analytic and time-steady models that assume pressureless freefall (e.g., O. Pejcha & T. A. Thompson 2012; M. J. Raives et al. 2018).
5. We explore the heuristic timescale ratio as an explosion condition (see Section 3.4). We find that the maximum value of the ratio of the advection time to the heating time in the gain region, i.e., the critical timescale ratio, varies along the critical curve. We also show that the critical timescale ratio depends on the definition of the advection

and heating timescales. We find that this ratio is below unity for near-critical stable models, it increases with $\mathcal{M}$, and it converges toward the limit of pressureless freefall (see Section 3.4 and Figure 12). Depending on $\mathcal{M}$, the critical timescale ratio varies by a factor of two or three along the critical curve.

6. We also explore the integral FEC, as quantified by $\tilde{\Psi}$ (Equation (33)). As with other explosions conditions, the critical value of $\tilde{\Psi}$ is a function of both $\mathcal{M}$ and $\dot{M}$ (see Section 3.5), but it converges as the limit of pressureless freefall is approached (see Figures 15 and 16). Depending on $\mathcal{M}$, the critical value of $\tilde{\Psi}$ varies by about a factor of $\simeq$0.2–2 across the range of $\dot{M}$ we explore.
7. Using our fiducial inputs, the critical antesonic ratio shows the least variation along the critical curve ($\simeq$3%–5% depending on $\mathcal{M}$) compared to the heuristic timescale condition (a factor of 2–3 depending on $\mathcal{M}$) and the FEC (a factor of 0.2–2 depending on $\mathcal{M}$).
8. We find shock oscillations for stable accretion models at low $\dot{M}$ that complicate the identification of a single explosion condition. Shock oscillations produce corresponding changes in all diagnostic quantities. For example, they may generate maximum antesonic ratios that are temporarily above the critical value (see Figure 9). Similar variations occur in the heuristic timescale condition and in the FEC.

With this computational framework in place, our future work will address 2D and 3D models, where we can assess the role of multidimensional instabilities in changing the normalization and character of the critical condition. Further work must also be done to understand the role of $\mathcal{M}$ in mapping realistic progenitor structures to the critical condition.

Acknowledgments

We thank Tejas Prasanna and Matthias Raives for helpful discussions. We thank Matt Colemann for helpful input regarding Athena++. We acknowledge partial support from NASA grant No. 80NSSC20K0531.

Data Availability

The implementation of the EoS, the problem generator file to run the simulations using Athena++, and the data shown in this paper are available upon request.

ORCID iDs

David Pochik https://orcid.org/0000-0002-8310-0271
Todd A. Thompson https://orcid.org/0000-0003-2377-9574

References

Abdikamalov, E., Zhaksylykov, A., Radice, D., & Berdibek, S. 2016, MNRAS, 461, 3864
Abdikamalov, E., Huete, C., Nussupbekov, A., & Berdibek, S. 2018, Parti, 1, 97
Adams, S., Kochanek, C., Gerke, J., & Stanek, K. 2017a, MNRAS, 469, 1445
Adams, S., Kochanek, C., Gerke, J., Stanek, K., & Dai, X. 2017b, MNRAS, 468, 4968
Bethe, H. A. 1990, RvMP, 62, 801
Bethe, H. A., & Wilson, J. R. 1985, ApJ, 295, 14
Boccioli, L., Gogilashvili, M., Murphy, J., & O'Connor, E. P. 2025, MNRAS, 537, 1182
Bruenn, S. W., Mezzacappa, A., & Dineva, T. 1995, PhR, 256, 69
Burrows, A. 2013, RvMP, 85, 245
Burrows, A., & Goshy, J. 1993, ApJL, 416, L75
Burrows, A., & Lattimer, J. M. 1985, ApJL, 299, L19
Burrows, A., & Lattimer, J. M. 1986, ApJ, 307, 178
Burrows, A., Radice, D., Vartanyan, D., et al. 2020, MNRAS, 491, 2715
Burrows, A., & Vartanyan, D. 2021, Natur, 589, 29
Burrows, A., Wang, T., & Vartanyan, D. 2024, ApJL, 964, L16
Colella, P. 1990, JCoPh, 87, 171
Colella, P., & Woodward, P. R. 1984, JCoPh, 54, 174
Coleman, M. S. 2020, ApJS, 248, 7
Colgate, S. A., Grasberger, W. H., & White, R. H. 1961, AJ, 66, 280
Couch, S. M. 2013, ApJ, 775, 35
Couch, S. M. 2017, RSPTA., 375, 20160271
Couch, S. M., & Ott, C. D. 2015, ApJ, 799, 5
Fernández, R. 2012, ApJ, 749, 142
Fernández, R. 2015, MNRAS, 452, 2071
Fernández, R., Müller, B., Foglizzo, T., & Janka, H.-T. 2014, MNRAS, 440, 2763
Fernández, R., & Thompson, C. 2009, ApJ, 697, 1827
Ferreira, M., & Providência, C. M. C. 2021, PhRvD, 104, 063006
Gabay, D., Balberg, S., & Keshet, U. 2015, ApJ, 815, 37
Gerke, J., Kochanek, C., & Stanek, K. 2015, MNRAS, 450, 3289
Gogilashvili, M., & Murphy, J. W. 2022, MNRAS, 515, 1610
Gogilashvili, M., Murphy, J. W., & O'Connor, E. P. 2023, MNRAS, 524, 4109
Hanke, F., Marek, A., Müller, B., & Janka, H.-T. 2012, ApJ, 755, 138
Hanke, F., Müller, B., Wongwathanarat, A., Marek, A., & Janka, H.-T. 2013, ApJ, 770, 66
Janka, H. T. 2000, NuPhA, 663, 119
Janka, H.-T. 2012, ARNPS, 62, 407
Janka, H.-T., Melson, T., & Summa, A. 2016, ARNPS, 66, 341
Kochanek, C. S., Beacom, J. F., Kistler, M. D., et al. 2008, ApJ, 684, 1336
Kotake, K., Ohnishi, N., & Yamada, S. 2007, ApJ, 655, 406
Lentz, E. J., Bruenn, S. W., Hix, R.W., et al. 2015, ApJL, 807, L31
Mabanta, Q. A., & Murphy, J. W. 2018, ApJ, 856, 22
Mazurek, T. J. 1982, ApJL, 259, L13
Melson, T., Janka, H.-T., Bollig, R., et al. 2015, ApJL, 808, L42
Mezzacappa, A., Endeve, E., Messer, O. E. B., & Bruenn, S. W. 2020, LRCA, 6, 4
Müller, B., Melson, T., Heger, A., & Janka, H.-T. 2017, MNRAS, 472, 491
Murphy, J. W., & Burrows, A. 2008, ApJ, 688, 1159
Murphy, J. W., & Dolence, J. C. 2017, ApJ, 834, 183
Neustadt, J., Kochanek, C., Stanek, K., et al. 2021, MNRAS, 508, 516
Nordhaus, J., Brandt, T. D., Burrows, A., & Almgren, A. 2012, MNRAS, 423, 1805
Ott, C. D., O'Connor, E. P., Gossan, S., et al. 2013, NuPhS, 235, 381
Ott, C. D., Roberts, L. F., da Silva Schneider, A., et al. 2018, ApJ, 855, L3
Pejcha, O., & Thompson, T. A. 2012, ApJ, 746, 106
Prasanna, T., Coleman, M. S. B., Raives, M. J., & Thompson, T. A. 2022, MNRAS, 517, 3008
Qian, Y. Z., & Woosley, S. E. 1996, ApJ, 471, 331
Raives, M. J., Couch, S. M., Greco, J. P., Pejcha, O., & Thompson, T. A. 2018, MNRAS, 481, 3293
Raives, M. J., Thompson, T. A., & Couch, S. M. 2021, MNRAS, 502, 4125
Scheck, L., Kifonidis, K., Janka, H. T., & Müller, E. 2006, A&A, 457, 963
Stockinger, G., Janka, H.T., Kresse, D, et al. 2020, MNRAS, 496, 2039
Stone, J. M., & Gardiner, T. 2009, NewA, 14, 139
Stone, J. M., Tomida, K., White, C. J., & Felker, K. G. 2020, ApJS, 249, 4
Sukhbold, T., Ertl, T., Woosley, S., Brown, J. M., & Janka, H.-T. 2016, ApJ, 821, 38
Sukhbold, T., Woosley, S., & Heger, A. 2018, ApJ, 860, 93
Summa, A., Janka, H.-T., Melson, T., & Marek, A. 2018, ApJ, 852, 28
Suwa, Y., Yamada, S., Takiwaki, T., & Kotake, K. 2015, ApJ, 816, 43
Takiwaki, T., Kotake, K., & Suwa, Y. 2014, ApJ, 786, 83
Thompson, C. 2000, ApJ, 534, 915
Thompson, T. A., Burrows, A., & Meyer, B. S. 2001, ApJ, 562, 887
Thompson, T. A., Burrows, A., & Pinto, P. A. 2003, ApJ, 592, 434
Thompson, T. A., Quataert, E., & Burrows, A. 2005, ApJ, 620, 861
Timmes, F. X., & Swesty, F. D. 2000, ApJS, 126, 501
Toro, E. F., Spruce, M., & Speares, W. 1994, ShWav, 4, 25
Vartanyan, D., Burrows, A., Radice, D., Skinner, M. A., & Dolence, J. 2018, MNRAS, 477, 3091
Wang, T., & Burrows, A. 2024, ApJ, 962, 71
Wang, T., Vartanyan, D., Burrows, A., & Coleman, M. S. 2022, MNRAS, 517, 543
Woosley, S. E., & Heger, A. 2007, PhR, 442, 269
Woosley, S. E., Heger, A., & Weaver, T. A. 2002, RvMP, 74, 1015
Yamasaki, T., & Yamada, S. 2005, ApJ, 623, 1000
Yamasaki, T., & Yamada, S. 2006, ApJ, 650, 291